






Article

Comparison of Model-Based and Sensor-Based Detection of Thermal Runaway in Li-Ion Battery Modules for Automotive Application

Jacob Klink ^{1,*}, André Hebenbrock ¹, Jens Grabow ¹, Nury Orazov ¹, Ulf Nylén ², Ralf Benger ¹
and Hans-Peter Beck ³

¹ Research Center Energy Storage Technologies, Clausthal University of Technology, Am Stollen 19A, 38640 Goslar, Germany; andre.hebenbrock@tu-clausthal.de (A.H.); jens.grabow@tu-clausthal.de (J.G.); nury.orazov@tu-clausthal.de (N.O.); ralf.benger@tu-clausthal.de (R.B.)

² Battery Performance & Cell Development, Scania CV AB, 151 87 Södertälje, Sweden; ulf.nylen@scania.com

³ Institute of Electrical Power Engineering and Electrical Energy Engineering, Clausthal University of Technology, Leibnizstraße 28, 38678 Clausthal-Zellerfeld, Germany; hans-peter.beck@tu-clausthal.de

* Correspondence: jacob.klink@tu-clausthal.de

Abstract: In recent years, research on lithium-ion (Li-ion) battery safety and fault detection has become an important topic, providing a broad range of methods for evaluating the cell state based on voltage and temperature measurements. However, other measurement quantities and close-to-application test setups have only been sparsely considered, and there has been no comparison in between methods. In this work, the feasibility of a multi-sensor setup for the detection of Thermal Runaway failure of automotive-size Li-ion battery modules have been investigated in comparison to a model-based approach. For experimental validation, Thermal Runaway tests were conducted in a close-to-application configuration of module and battery case—triggered by external heating with two different heating rates. By two repetitions of each experiment, a high accordance of characteristics and results has been achieved and the signal feasibility for fault detection has been discussed. The model-based method, that had previously been published, recognised the thermal fault in the fastest way—significantly prior to the required 5 min pre-warning time. This requirement was also achieved with smoke and gas sensors in most test runs. Additional criteria for evaluating detection approaches besides detection time have been discussed to provide a good starting point for choosing a suitable approach that is dependent on application defined requirements, e.g., acceptable complexity.

Keywords: lithium-ion battery module; fault detection; thermal runaway; thermal fault; external heating; battery safety



Citation: Klink, J.; Hebenbrock, A.; Grabow, J.; Orazov, N.; Nylén, U.; Benger, R.; Beck, H.-P. Comparison of Model-Based and Sensor-Based Detection of Thermal Runaway in Li-Ion Battery Modules for Automotive Application. *Batteries* **2022**, *8*, 34. <https://doi.org/10.3390/batteries8040034>

Academic Editors: Binghe Liu, Lubing Wang, Yuqi Huang, Yongjun Pan and Carlos Ziebert

Received: 1 March 2022

Accepted: 7 April 2022

Published: 12 April 2022

Publisher's Note: MDPI stays neutral with regard to jurisdictional claims in published maps and institutional affiliations.



Copyright: © 2022 by the authors. Licensee MDPI, Basel, Switzerland. This article is an open access article distributed under the terms and conditions of the Creative Commons Attribution (CC BY) license (<https://creativecommons.org/licenses/by/4.0/>).

1. Introduction

The increasing demand on lithium-ion batteries in recent years—mainly spurred by automotive applications [1]—is accompanied by rare fire incidents with disproportionate supra-regional attention with respect to the smaller incident frequency compared to vehicles with combustion engines [2]. Besides the customers' loss of confidence in the safety of electromobility and the risk of property damage and personal injury, these accidents repeatedly lead to extensive recall and inspection campaigns—proactive or government-imposed (Boeing 787 [3], Samsung Note 7 [4], Electric buses in Germany [5] or Chevrolet Bolt [6])—causing financial and reputative damage to the manufacturer [7]. In addition, recent battery cells are developed under the need for high energy and power density, which also results in more available energy in case of failure. Thus, battery safety is still considered as one of the greatest challenges in battery technology [8] and a key aspect for the safe operation of high-power battery storage systems.

The failure of lithium-ion cells is well-described [9] and characterised by extensive exothermic side reactions of cell components that result in a self-accelerating loop until

the remaining energy is released mostly in an explosion-like event. This failure process is commonly named as *Thermal Runaway* [10]. However, the definition of Thermal Runaway is not harmonised [8,11] and varies between the state of a thermal imbalanced system [12] and precise process states. For the latter, e.g., Li et al. has defined 90 °C [13] while either $T \geq 350 \text{ °C}$, $\Delta U \geq 0.5 \text{ V}$ or $\frac{dT}{dt} \geq 10 \text{ K min}^{-1}$ has been utilised in [14], where ΔU represents a sudden voltage drop relative to a fault-free condition. Furthermore, Thermal Runaway definitions based on the characteristic behaviour of self-heating, release of gases and particles and explosion [15] are documented as well. Within this paper, the latter descriptive definition is used.

As battery systems consist of hundreds to thousands of cells, such an explosive energy release usually causes adjacent cells to fail as well. Thus, this phenomena of propagating a single cell fault to further cells is labelled as *Thermal Propagation* in the literature. Since the amount of released energy accumulates with each additional cell failure, this process endangers bystanders and the environment much more than the individual Thermal Runaway.

To reduce these risks, three approaches are mainly identified in the recent literature:

1. Increasing the thermal stability of cells by alternative active materials or additives, as extensively summarised by Tidblad et al. [16] or Liu et al. [17].
2. Decreasing the heat transfer from cell to cell by constructive changes [18,19], active or passive cooling [20,21] and/or thermal isolation [22] to slow down or rather stop Thermal Propagation and increase warning and evacuation times. This approach is in agreement with the US *Vehicle Battery Safety Roadmap Guidance* that states Thermal Propagation must not occur [23], acknowledging the imminent risk of one-cell faults [7].
3. Early detection of battery faults to provide warning and evacuation time, which is also the subject of this work. In this context, the Global Technical Regulation on Electrical Vehicle Safety (GTR-EVS) specifies at least a 5 min pre-warning time [24].

Based on the aforementioned description of Thermal Runaway, a variety of measured variables with dependence on the fault condition are conceivable for detection, as listed in Table 1. Due to the complexity of the electrochemical system, however, overlapping with the other, non-safety-relevant processes and typical safety devices must also be taken into account to minimise false-positive detection. In addition, the time of detection is highly dependent on the underlying process, as indicated by the given temperature ranges.

Table 1. Selection of measurement variables to describe the presence of Thermal Runaway.

Process Variable	Dependency of Thermal Runaway Processes	Other Dependencies
Gases	After cell rupture: Electrolyte vaporisation and gas producing reactions (see internal pressure) Gas released approx. 0.9 L/Ah to 3.5 L/Ah [25] at 25 °C, 1 bar	Pre-cell rupture: Electrolyte leakage [26] SOC and chemistry [27] Ageing (at different conditions) [28] Atmosphere and oxygen availability [29] Type of trigger [30]
Impedance	Increasing temperature by exothermic reactions cause decreasing impedance and change of phase [31]; inverse behaviour for high temperatures [32] Safety Device Shutdown-separator cause ΔR of 1300% [33] usually at 120 °C to 150 °C [34]	SOC [31,35] Temperature of operation Cyclic Ageing [36,37] Calendrical Ageing [7]

Table 1. Cont.

Process Variable	Dependency of Thermal Runaway Processes	Other Dependencies
Internal pressure/strain	Thermal expansion Electrolyte evaporation and gas producing reactions[38]: – CO ₂ by SEI decomposition [39] at 90 °C to 120 °C [40] – C _x H _y by SEI-reformation [41] at 120 °C to 218 °C [34] Safety device: burst-disc rupture approx. at 10 bar to 12 bar for prismatic cells [42]; deviation with 18650 cells $\sigma \leq 5\%$ [43]	SOC and load [44,45] Ambient pressure [46] Temperature of operation Gas formation during ageing [7]
Smoke/particles	After cell rupture: Vaporisation (<i>White smoke</i> [47]) and combustion of cell components (<i>Black smoke</i>) [38]. Ejection of internal cell components (<i>Black smoke</i>) [15,47]	Ambient atmosphere
Temperature	Increasing internal temperature due to exothermic reactions	Load [48] and cooling situation [49,50] Temperature of operation
Voltage	Increasing temperature as $OCV = f(T)$ [51] Melting of separator: – PE = 120 °C to 135 °C, PP = 150 °C to 166 °C [34,40,52] Safety Device: CID, OSD, Shutdown-separator 120 °C to 150 °C [34]	SOC Over-voltages during load

Despite the various signals, the vast majority of papers on the detection of cell faults, as recently summarised by Hu et al. [53], mainly build their methods on voltage and eventually surface temperature measurement—independently if the main principle comes from statistical outlier detection [54], neural networks [55] or modelling [56]. Other signals, such as strain and internal temperature, e.g., measured by optical fibre, as proposed by Zhu et al. [57] and Nascimento et al. [44], have been published for describing the development of Thermal Runaway in general instead of fast fault detection. In contrast, such signal-based approaches are already documented in patents such as H₂ and CO monitoring in [58].

It has to be mentioned that there is extensive research on characterising the development of Thermal Runaway by multiple quantities, e.g., by Finegan et al. in [59,60]; on the other hand, however, the results are neither investigated under the scope of fault detection nor considered within detection-focused studies to give context for the achieved results. Due to this development, a well-founded assessment of different measurement parameters and detection methods for use in automotive applications is currently only possible to a limited extent. In addition, current research is often limited to small lab-size battery modules, which is significantly differentiating from the size and quality of battery modules used in automotive applications, and mainly focused on internal short circuits (see review [53]). Thermal faults as the second type of failure, on the other hand, are only investigated in few studies, such as [61]. Approaches like those presented in [62–66] utilise real vehicle data from selected field-failures, ensuring to investigate relevant faults; however, the lab-advantage of controlling the boundary conditions is not given.

The first approach on this gap was conducted by Koch et al. [67], comparing the readings of a variety of different sensors during the Thermal Runaway of modules triggered by multiple methods with respect to detection possibilities.

This study aims to build on that work by rerunning a similar sensor setup on an automotive battery case in comparison to a model-based detection method from our previous work [68]. By this, the change of impedance should be incorporated as well. The test setup was designed to be as close as possible to the application, thereby using original battery modules, battery housing and operation boundaries from an all electric (BEV) heavy duty trucks by Scania. External heating at two rates was chosen as the trigger to represent

an over-time-developing fault condition. To improve the significance of the results, each test was conducted twice.

The content of this paper is structured as follows: In Section 2, the experimental setup of module and sensors are given, followed by the test setup and design of model-based detection. The results of the experimental tests are described and discussed in Section 3 with a focus on the repeatability in between tests before analysing the individual sensors and a comparative evaluation of detection feasibility. The main findings are summarised in Section 4.

2. Materials and Methods

2.1. Material

For the conduction of the abuse tests on a module/system level, both preparations of the device under test (DUT) and of multiple sensors for monitoring the different quantities, as described in the following, were performed.

2.1.1. Device under Test

As DUT, automotive battery modules based on prismatic cells of type PHEV2 [69] were used (Please understand, some details on the cells are in conflict with confidential information due to the proximity to automotive production). The module is commercially available and the cells contain NMC-based chemical constituents commonly employed in BEV vehicles today. Each module consists of twelve cells that are configured in a side-by-side 12s1p-setup, as pictured in the upper left section of Figure 1. The real appearance of the module can be seen in the embedded photo also in Figure 1. According to the manufacturer, the individual cells are equipped, among other things, with an overcharge-safety-device (OSD), creating an internal short circuit between the cell terminals when the cell pressure surpasses a (not published) threshold, as described in patent US 10.026.948 B2 [70], and disconnects the active parts from cell terminals. Thus, the cell is electrically bypassed from the load current. Furthermore, a vent for the release of internal over-pressure is implemented into the cell—hereinafter referred to as burst-disc. The position of the burst-disc is indicated by the light-colour area behind the cell numbers in Figure 1.

Please note the nomenclature given in the schematic—numbering the cells from the positive terminal (C01) towards the negative terminal (C12). For simplification, this naming convention is adopted to the associated measurements in the following; for example, T_{01} represents the temperature on top of cell C01.

For the individual tests, identical brand-new modules were utilised. The modules were equipped with the original cell management controller (CMC) that is used in real application as the responder within the whole battery management system (BMS). For a detailed differentiation between CMC and BMS, please refer to [71]. In preparation for the experiments, the modules were tempered at 25 °C and cycled two times using a constant current–constant voltage (CC–CV) protocol for the charge and CC protocol for the discharge direction. The cycles were performed within the given cutoff limits by the manufacturer and at a maximal current of $C/3$. In accordance with most similar test protocols, the CV phase was terminated when the current fell below $C/20$. Using this CC–CV protocol, the DUT were charged, subsequently representing 100% state of charge (SOC), and after a relaxation period of 30 min, the initial state of SOC_{upper} was reached by discharging with $C/3$.

As displayed in the lower inset of Figure 1, the battery module consists of cells encapsulated by an aluminium casing in an original state. For placement of the heating device described below, the cover on the head-end at the side of the positive terminal of this aluminium casing was removed. After the installation of the heater with direct contact to cell C01, both the thermal contact between the heater and cell and the pre-tension of all cells were guaranteed by two steel strapping tapes.

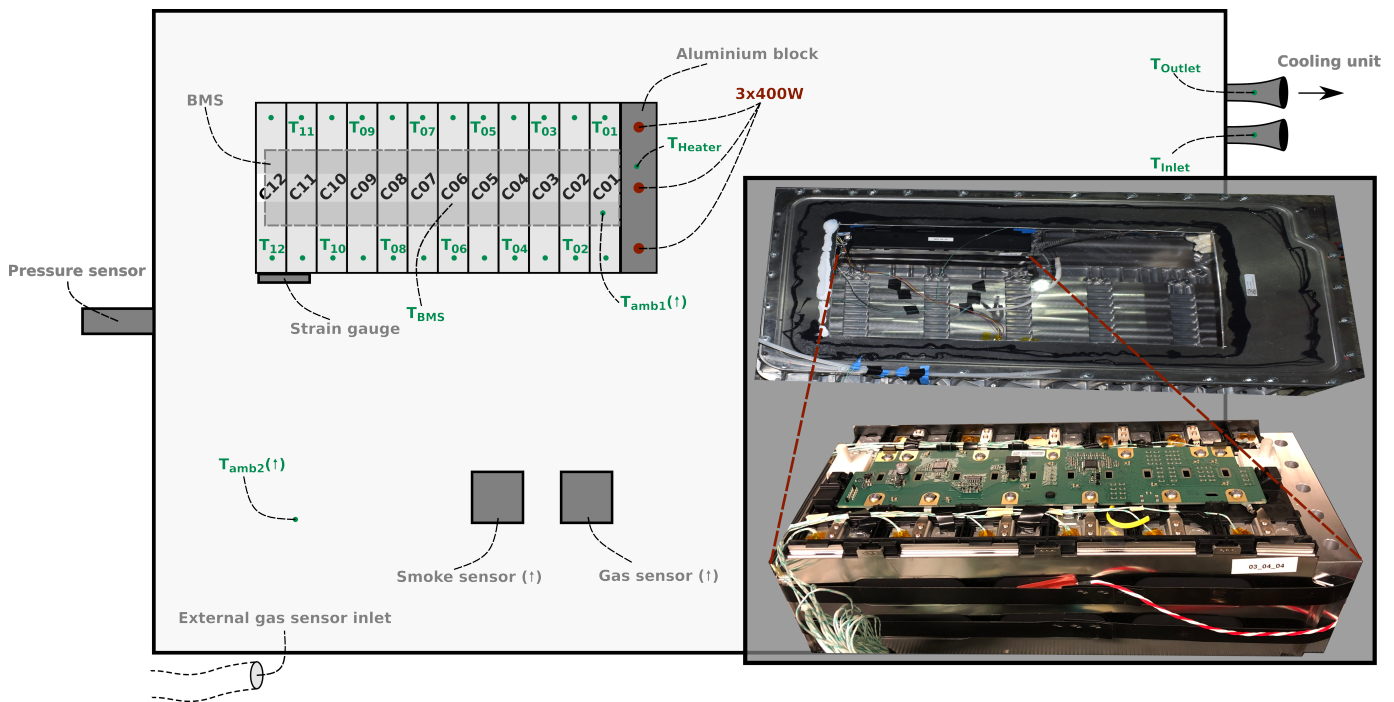


Figure 1. Main figure: Position of module and placement of sensors within battery case (not to scale). Sensors placed inside the battery case at the lid are marked by an arrow (\uparrow). For detailed sensor information, please refer to Table 2. Photo inset: Prepared battery case (top) and modified module with attached aluminium block (bottom).

Each DUT was placed and screwed in the top left of the original aluminium battery system housing designed for eight modules in total, as visualised in the upper photo in Figure 1. In the application, eight modules will be screwed to the battery system housing, as indicated by the polished foundations in the photo. In this configuration, the modules are separated by a small distance. Through a combination of multiple battery systems, the required electrical properties are achieved. The system case comes with an aluminium lid and gasket screwed on top in addition to several openings in the side for items like cable entries or pressure discs. In addition, channels for cooling fluid from an external thermal management are located in the bottom plate of the housing. For the experiments, a window of polycarbonate-glass was added to the lid, providing vision towards the DUT during the test. To restore the gas-tight original state, the window was properly sealed with silicon and mounting adhesive. For the same reason, all openings were closed with polyurethane foam after the installation of all cables.

2.1.2. Sensors

The variety of sensors used in this study are summarised in Table 2 with the respective quantity. In addition, the utilised sample rate of each sensor is also given together with the layer of measurement. Please refer to Figure 1 for a visualisation of the sensor location in relation to the module and heater placement inside the battery case. The external sensor set is extended by the capabilities of the CMC to represent the close-to-application available data set.

Table 2. Measured quantities, utilised sensors, sensor positions and corresponding sample rates. For detailed information on locations please refer to Figure 1.

Quantity	Sensor/ Logger	Sample Rate	Location
Voltage	Gantner Q.station XB	10 Hz	Cell-level
	CMC	10 Hz	Cell-level
Current	EA Power Supply PSI 10000	10 Hz	Module-level
	Fluke i400s, Gantner Q.station XB	10 Hz	Module-level
	EA Power Supply PSI 10000	10 Hz	Module-level
Temperature	CMC	10 Hz	C06
	Pico TC-08	1 Hz	12× cell-level
			1× heating device 2× ambient battery case 1× inlet and outlet of cooling fluid
Vapour/particles	MaximIntegrated MAX30101	≈4 Hz	System case
Gases	Sensirion SGP40	≈1 Hz	System case
	Dräger X-am 8000	1 Hz	System environment
Pressure	RS Pro IPS (7975043)	5 kHz	System case
Strain	Micro-Measurement 500UW	1.25 Hz	Module-level

The data acquisition was performed using the data loggers and data processors suitable for the sensors selected, with either analogue or digital signal outputs. The data loggers were placed outside the test environment, as a result of which reliable data acquisition was possible while sensors and cables were functional. All devices were synchronised to an online time server for later time-synchronising on the logged timestamps. The achieved synchronisation was validated by the redundant measurement of the current and voltage across multiple loggers.

Voltage was logged on the cell level externally by a data logger and by using the mounted CMC. For the latter, the data acquisition was realised by a custom debug functionality that was implemented by Scania for CAN communication. Both external and integrated voltage monitoring were screwed to the same point-of-contact on the cells. Additional voltage monitoring and logging were conducted by the utilised power supply at the module level. Since no separate sense cable was used, the actual value is regarded as biased but provides an opportunity for verification of the synchronisation.

Current was primarily logged by the power supply itself but was supplemented using a current probe with the voltage data logger for redundancy and synchronising. Since the cells of the DUT were connected in a serial connection, the module-current measured at the power supply was equal to the cell current.

Temperature has been monitored on the cell level at the positive terminal of each cell using type K thermocouples with welded tips. These sensors were electrically isolated from the surface as well as glued to position with Kapton[®] tape. The same type of sensors was used for the measurement points $T_{amb1,2}$. In contrast, both the heater temperature T_{Heater} and cooling fluid temperature (T_{Inlet} , T_{Outlet}) were measured using type K metal sheath thermocouples. For the fluid temperature, the sensor tips were positioned approximately centre in the tube. An additional sheath thermocouple was implemented close to T_{Heater} , providing the actual temperature for the heater controller (see below). The cables of the latter sensors were thermally protected by a high temperature-resistant furnace sealing strip. In addition to the aforementioned external sensors, the module temperature monitored internally by the CMC was logged as well. Please refer to Figure 1 for the position of the corresponding thermistor at C06.

Smoke detection, specifically vapour and particles in the atmosphere inside the battery case, was implemented based on an integrated circuit board with infrared functionality. Here, the measurement principle is based on the reflection time of an emitted infrared beam that allows for the evaluation of the atmosphere properties in front of the diode. Due to

the simple measurement setup, the evaluation is a qualitative rather than quantitative gas assessment like gas amounts or further—lab-quality—analyses as particle size distribution. The measurement signal is proportional to the particle-free distance in front of the sensor; thus, the value can indicate the amount of smoke but is also influenced by the position of the sensor relative to the smoke emitter. For the sake of simplicity, this measurement of vapour and particles will be referred to as smoke sensor in the following sections.

Gases inside the battery case were also measured using an integrated circuit board—in this case, based on a metal-oxide sensor for air quality. Thus, the sensor is sensible for hydrogen H_2 and hydrocarbons C_xH_y that are summarised in the following sections by volatile organic compounds (VOC). In addition to the raw signal gathered from the metal-oxide sensor, the chip also calculates, internally, an air quality index. Both smoke and gas sensors are similar to the setup described by Koch et al. [67]. Further gas measurement was implemented outside the battery case using a mobile gas-sensing unit by Dräger to assess the quality of the achieved case sealing. For this purpose, the air-intake was placed directly beside the lid-sealing in the flow-direction of the air inside the test chamber due to the exhaust gas extraction. By this measurement position, the reading can also be utilised as the worst-case estimation of the gas exposure for bystanders during Thermal Runaway and potential Thermal Propagation.

Pressure that builds up inside the enclosed battery case relative to ambient atmosphere is monitored using a piezo-based sensor. The sensor was screwed into the modified aluminium casing close to the triggered battery module, as visualised in Figure 1. As a result of the experience from previous abuse tests, the sample rate was set to 5 kHz since very short pressure peaks have used to be observed. The upper sensor range is 1 bar above the reference pressure.

Strain of the module was measured by a strain-gauge that was glued onto the two metal strapping tape, as mentioned above. Here, the upper tape was prepared beforehand, thereby guaranteeing at least 24 h curing time for a reliable connection.

Due to the energy release during each test, the destruction or damage of the sensors inside the battery case has been expected with the exception of the pressure sensor. Therefore, each DUT was prepared using a new set of sensors.

2.1.3. Load

The electrical load of the module during the abuse tests was provided by the above mentioned power supply PSI 10000, controlled and monitored by a custom LabVIEW®-program. With this setup, the power supply target value was actualised according to a given current profile at 10 Hz rate within the preset module safety limits.

During the operation, cooling fluid was circulated within the cooling channels in the bottom plate of the battery case. The fluid temperature was controlled by the ECO E 10 S cooling unit from Lauda, capable of both heating and active cooling. In combination with a separate pump, a fluid velocity of 4 L min^{-1} was achieved. This value is within the flow-velocity range of the real automotive application of the battery case. At this flow rate, the area heat transfer coefficient from cell to cooling fluid was experimentally determined from 100 W K^{-1} to 130 W K^{-1} .

For triggering the thermal-induced failure, a heating device was mounted at the head end of cell C01 of each module. This heating block has the same dimensions as the cells and was manufactured from aluminium with mounting positions for three heating cartridges, as visualised in Figure 1. Heat cartridges with a nominal power of 400 W each were connected in parallel to 230 V, providing a peak power of 1200 W in total. By a PID-controller that was pre-tuned on this test-setup, phases of constant temperature as well as ramps with a constant temperature rate were realised.

2.2. Method

2.2.1. Experimental

The preconditioned and mounted modules (see above) were placed within the abuse test-chamber that provides a safe test environment, with features such as active smoke extraction and purification. The battery housing was elevated from the ground to avoid unrealistic heat loss. By activating the thermal management at least 30 min before the abuse test, a steady state at the beginning of the experiment was guaranteed. According to the module data sheet, the thermal management was set to 25 °C as the operation temperature. The ambient temperature outside of the battery case was highly dependent on the outside temperature at the test site in northern Germany during October due to the active smoke extraction. Thus, the thermal management regulates the module temperature during pre-heating by heating and cooling during the thermal fault operation.

During the experiment, the module was electrically cycled with a dynamic drive profile, providing both charge and discharge periods. Instead of the often utilised synthetic dynamic profiles, the data were collected at 10 Hz rate beforehand on board of an electric heavy duty truck, driving through a mixed urban–rural area, with a total duration of approximately 3600 s. In comparison, the world harmonised vehicle cycle (WHVC) [72] application lasts 1800 s. A detailed comparison between the utilised cycle and the WHVC or other popular test specifications is not performed as the characteristics of the synthetic profiles highly depend on the used transformation from the velocity profile to the power or current cycle.

To increase the length of the load profile, the measured data were concatenated twice and a CC-charging phase was added at the end, resulting in a maximal test duration of 10,200 s, or rather, 170 min. The full profile relative to the module capacity is visualised within Figure 2, as well as the corresponding SOC initialised at SOC_{upper} .

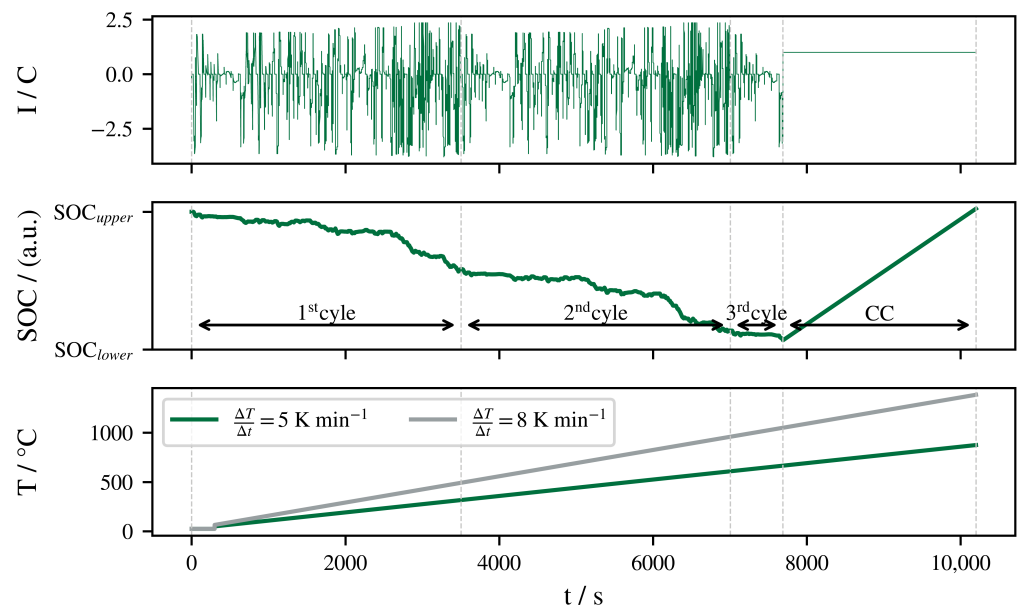


Figure 2. Change of SOC of module by dynamic electrical test profile with initial state SOC_{upper} . Synchronous thermal fault trigger with either 5 K min^{-1} or 8 K min^{-1} after 5 min of test.

To get a baseline of the voltage measurement and the implemented strain sensor, one module was cycled using this profile at a regulated 25 °C inside a climatic chamber.

For the investigation of the abuse behaviour, the attached heating device (see above) was activated during dynamic load. The PID-controller was set to a 5 min pre-warming phase at a constant 25 °C followed by continuous heating with a constant temperature slope. Besides a heating rate of 5 K min^{-1} that can be found in several test manuals,

e.g., IEC 62600-2 and UL 2580 (see Ruiz et al. [73]), a faster heating rate with 8 K min^{-1} was investigated as well. The latter rate was chosen to consider the test requirements by FreedomCAR of 5 K min^{-1} to 10 K min^{-1} [73]. Due to the faster heating, a smaller pre-warning time was expected, thereby representing a more critical fault situation for the investigated approaches. The described thermal trigger definition is also displayed within Figure 2. With respect to the displayed final temperature of the heating device for both test variations, it was expected that the triggered cell C01 would suffer Thermal Runaway significantly before the end of the test cycle. Thus, the module-SOC at failure would be within the operational range.

Previous studies, e.g., [47,74], have identified various critical boundary conditions and disturbing influences altering the achieved results from abuse tests. To identify such disturbing influences—if present—and for the evaluation of the result validity, both test setups were repeated once, as proposed by [40]. An overview of the described test specifications is given in Table 3.

Table 3. Test setup and nomenclature of individual abuse tests.

	A	B	C	D
Heating rate	5 K min^{-1}	5 K min^{-1}	8 K min^{-1}	8 K min^{-1}

The monitoring of the sensors listed in Table 2 began before the start of the load with the exception of the pressure sensor to minimise the file size. However, when the triggered cell (T_{01}) reached $80 \text{ }^\circ\text{C}$, the logging was manually started. In addition, the heating unit was deactivated when either T_{01} had surpassed $150 \text{ }^\circ\text{C}$ or Thermal Runaway had been observed. The electrical load was deactivated when the remaining module voltage fell below the minimal operational voltage.

2.2.2. Model-Based Fault Detection

To define a baseline for detection time without additional sensors, the model-based method, principally from our previous work [68], was employed. By modelling the battery behaviour under normal conditions, the cell-level voltage measurement can be set in contrast and potential deviations can be detected. The main structure of this fault detection method using a parallel observer-like model can be found in Figure A2 in the Appendix A. The feasibility of this method is made possible by the temperature-dependence of the cell impedance and the resulting change of the internal over-voltages when heated, as indicated in Table 1. To ensure early detection, a precise simulation of the normal behaviour at different temperatures and SOC is mandatory.

The model structure was kept similar to the previous work, as described in the following sections, and implemented in Matlab[®]/Simulink [75]. Please find additional information on the model setup in the Appendix A.

As commonly chosen as the best compromise between accuracy and computational effort [76], a second order equivalent circuit model was utilised for the electrical part, see Figure A1. The dynamic voltage behaviour $U_{cell}(t)$ of this model is described by Equation (1) where OCV represents the open circuit voltage, I the load current ($I \geq 0 :=$ charging) and R_i, C_i are equivalent resistances and capacities, respectively. Current direction, SOC and temperature were considered as influences for the cell parameters R_i and C_i , whereas OCV was implemented as $f(SOC, \alpha)$. Here, α is a correction factor to incorporate the hysteresis of the open voltage behaviour, as described in [77].

$$U_{cell}(t) = OCV + I \cdot \left[R_0 + \sum_{i=1}^{i=2} R_i \cdot \left(1 - \exp \frac{-t}{R_i \cdot C_i} \right) \right] \quad (1)$$

The OCV characteristics were defined at $25 \text{ }^\circ\text{C}$ in between 100% to 0% by averaging the static voltage measurement. In addition, the cell parameters were identified by fitting

the dynamic pulse test data onto Equation (1) for ranges of approximately $-20\text{ }^{\circ}\text{C}$ to $40\text{ }^{\circ}\text{C}$ and 10% to 90% SOC for each current direction. Within the model, the parameters were implemented as look-up-table.

To track the internal temperature of the cell jelly roll for electrical parameter identification, a simplified thermal model based on concentrated thermal masses was utilised. On the basis of extensive simulation data by the involved automotive manufacturer Scania, heat transfer mechanisms—except by conduction towards the cooling plate at the bottom—were neglected. Based on these prerequisites, two system states T_{cell} and $T_{terminal}$ were defined representing the active cell parts (jelly roll) and the cell terminal as the location of temperature measurement, respectively. The temperature of the cooling fluid T_{fluid} was set as the constant system boundary. During the load, the heating power \dot{Q} is defined by the electrical over-voltages, as shown in Equation (2). Please find the corresponding equivalent circuit structure in Figure A1 in the Appendix A.

$$\dot{Q} = I \cdot (U_{cell} - OCV) \quad (2)$$

The thermal parameters were parameterised based on material dimensions and properties, as well as heat gradient tests performed internally by Scania.

For fault detection, the model output was continuously compared with the individual cell voltages measured by the CMC. The difference was then subject to fault assessment. At reference tests under normal conditions, this signal had very short but high peaks that would have required to rise the detection threshold significantly. As this behaviour is most likely caused by measurement asynchronicities of the CMC or not sufficiently captured dynamics of the model, a small delay was added to the signal evaluation. Therefore, the threshold had to be exceeded for $t \geq 0.5\text{ s}$ to trigger the fault detection. Based on the reference measurements with the same electrical load, the threshold was set to -20 mV to 60 mV .

3. Results and Discussion

With all four test setups of Table 3, the cell C01 was successfully triggered to Thermal Runaway within the duration of the previously defined test cycle. However, it has to be mentioned that within Test D, the power of the electrical load was limited in charging direction by accident. Due to this limitation, the maximum charging current was $\approx 0.25\text{ C}$ instead of the given value of $\approx 2.4\text{ C}$ in Figure 2. Nevertheless, in all cases, the cell failure of the first cell was propagated to the adjacent cells, resulting in full thermal propagation of the battery module. However, a detailed discussion of the propagation characteristics was outside the scope of this paper on fault detection *before* the first Thermal Runaway.

As Thermal Runaway tests are often criticised for poor repeatability [8], the similarity between the tests performed is briefly discussed in the following paragraph. The development of the different sensor readings are subsequently presented and approaches for fault identification are discussed. As mentioned above, all measurements were synchronised based on the logged timestamps. For better comparability, all times are referred to as the start time of the heating device in seconds, starting at zero (0 s) in the following analysis.

3.1. Development of Thermal Runaway

The temperature and voltage measurements of abuse Test A are displayed in Figure 3. In contrast to the above-mentioned extensive sensor locations, only a few selected measurements are presented for clarity. Here, T_{01} and U_{01} as well as T_{12} and U_{12} as the cells closest to and most distanced to the heater, respectively, were chosen. In addition, the temperature of the heating device T_{Heater} and the sensor of the CMC T_{CMC} are presented. Within the tests, four characteristic events were identified:

- ① Begin of heating. Defined by temperature T_{Heater} .
- ② Activation of OSD-device. Defined by sudden loss of U_{01} readings.
- ③ Rupture of burst-disc. Defined by pressure measurement, visually validated.

- ④ Thermal Runaway. Defined by a sudden increase in temperature T_{Heater} and T_{01} , visually validated.

The timings of these events during the experiment are also annotated in Figure 3 by vertical dashed lines. In addition, selected temperature readings at these events are summarised in Table 4 for all four tests conducted.

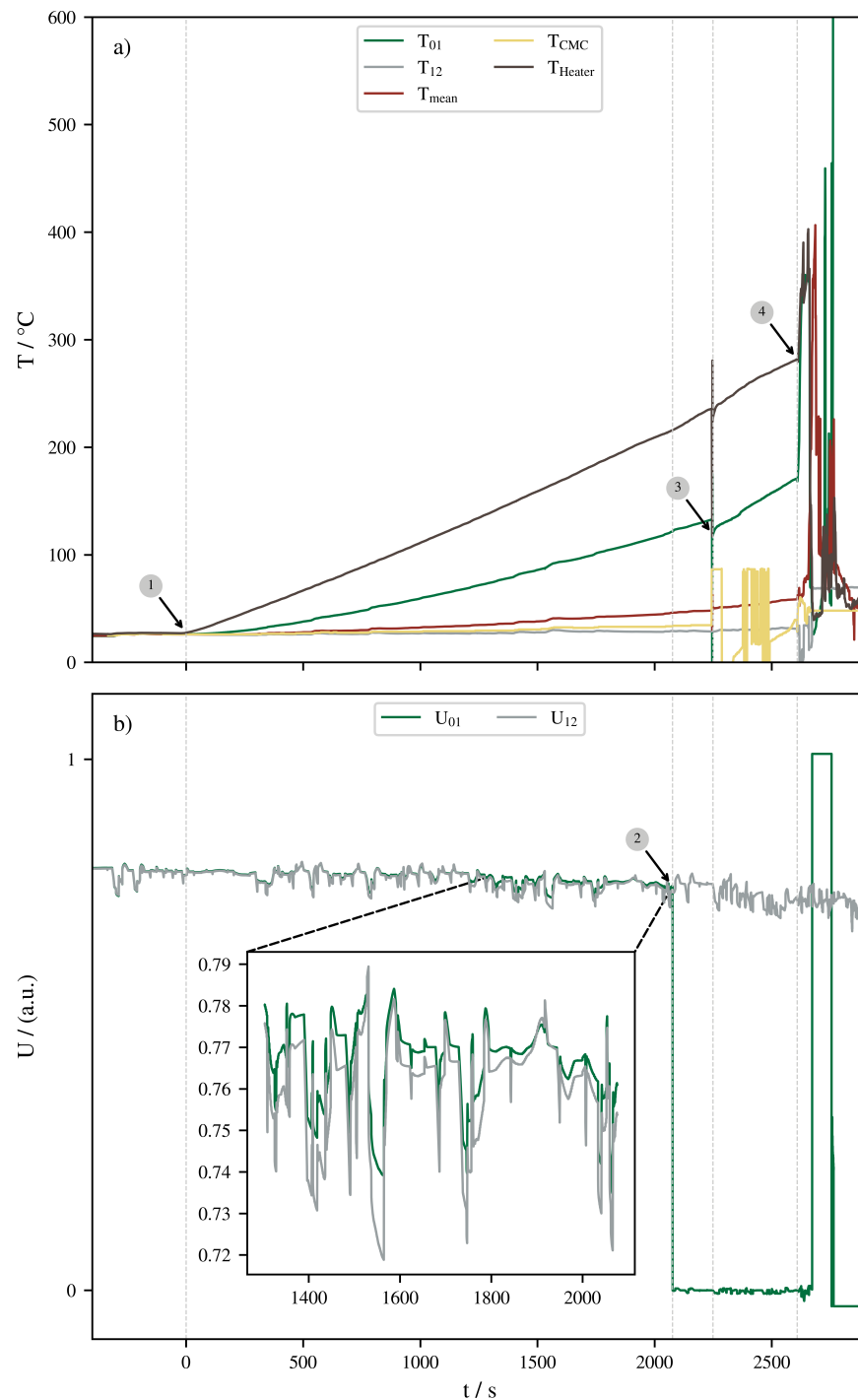


Figure 3. Development of Thermal Runaway due to external heating by characteristic events. ① Start of heating. ② Activation of OSD-device. ③ Rupture of burst-disc. ④ Thermal Runaway. (a) Temperature measurements and module average T_{mean} . Please refer to Figure 1 for sensor position. (b) Cell voltages C01 and C12 as the hottest and the coldest cells, respectively.

Table 4. Duration for reaching characteristic events by external heating with 5 K min^{-1} (A,B) and 8 K min^{-1} (C,D). Externally measured temperatures T_{01} , T_{12} and T_{Heater} , as well as a reading from CMC at time of event. ① Start of heating. ② Activation of OSD-device. ③ Rupture of burst-disc. ④ Thermal Runaway. Potential measurement error marked in red.

		A	B	C	D
①	t	0.00 s	0.00 s	0.00 s	0.00 s
	T_{CMC}	26.00 °C	25.00 °C	24.00 °C	24.50 °C
	T_{01}	26.26 °C	24.69 °C	23.97 °C	24.36 °C
	T_{12}	25.96 °C	25.27 °C	24.68 °C	24.89 °C
	T_{Heater}	27.49 °C	NaN °C	25.84 °C	25.68 °C
②	t	2076.00 s	2138.00 s	1449.00 s	1518.00 s
	T_{CMC}	33.50 °C	32.50 °C	29.50 °C	29.50 °C
	T_{01}	121.61 °C	120.75 °C	119.05 °C	123.27 °C
	T_{12}	29.13 °C	29.03 °C	26.95 °C	27.50 °C
	T_{Heater}	215.82 °C	NaN °C	236.16 °C	252.65 °C
③	t	2249.00 s	2297.00 s	1549.00 s	1611.00 s
	T_{CMC}	86.50 °C	27.56 °C	86.50 °C	86.50 °C
	T_{01}	118.41 °C	132.30 °C	129.47 °C	135.74 °C
	T_{12}	28.64 °C	29.78 °C	27.29 °C	28.80 °C
	T_{Heater}	227.06 °C	105.10 °C	14.62 °C	248.58 °C
④	t	2608.00 s	2640.00 s	1748.00 s	1874.00 s
	T_{CMC}	32.09 °C	30.50 °C	30.54 °C	18.96 °C
	T_{01}	169.84 °C	30.06 °C	159.84 °C	NaN °C
	T_{12}	31.11 °C	32.19 °C	30.27 °C	28.30 °C
	T_{Heater}	281.79 °C	NaN °C	282.19 °C	562.07 °C

Approximately 300 s into the dynamic profile, the start of the linear heating ramp (①) can be identified in the signal of T_{Heater} , causing a linear temperature increase in the adjacent C01. A slight offset and smaller rate is observed due to heat transfer resistance and thermal mass. With more distance to the heating device, as valid for cells C02–C12, additional thermal capacities and thermal transfer resistances are added along the module. Thus, the heating of further cells is delayed, causing a temperature difference as visible between T_{01} and T_{CMC} or T_{12} . To display the great deviation in temperature, the mean module temperature T_{mean} is also given. During the heating of C01, the mean temperature is found to be significantly smaller than T_{01} . As the heating proceeds, an increasing deviation between the voltage measurements of C01 and C12 is identified—especially visible within the zoomed part of Figure 3. As influenced by the temperature the most, U_{01} shows greater values than the approximately unaffected U_{12} . This observation is in accordance to previously published experimental results on cell level (see [68]) and the above-described (Table 1) inversely proportional temperature dependency of cell impedance—as the impedance decreases, the internal over-voltage decreases as well.

No temperature development greater than normal fluctuation was observed for both the cooling fluid temperatures T_{Inlet} , T_{Outlet} and ambient temperatures $T_{amb1,2}$ during the experiment towards the first Thermal Runaway. Therefore, these readings were excluded from further evaluation.

Subsequently, a sudden loss of the voltage reading of C01 is identified in Figure 3 when the OSD safety device was triggered (②) due to the built up internal cell pressure, creating a short circuit between both cell terminals. Shortly after this, the rupture of the burst-disc is observable (③). This event causes a short cooling effect as visible in the measurement of T_{01} at the annotation of ③ in addition to a slight release of white smoke into the battery case. Please refer to Figure A3b in the Appendix A for a depiction of this moment by photo. Besides the release of hot gases, this cooling effect is also caused by the evaporation enthalpy, as identified by Qin et al. [78].

Unfortunately, within all four tests, the temperature sensors were mounted close to the heating device and the triggered cell temporally malfunctioned at the same time of cell rupture. The readings jumped arbitrarily between higher (eventually plausible), smaller (plausible due to cooling) and negative (not plausible) values, as well as reference cold-junction temperature ($\approx 10^\circ\text{C}$ to 20°C) and no reading at all. However, since the measurements recover to reasonable values, the main description of the Thermal Runaway is not affected. Please note that the measurements that are most likely to be influenced by this sensor malfunction or due to sensor-destruction by Thermal Runaway are highlighted in Table 4 in red colour.

Shortly after the burst-disc rupture, significant smoke development—starting white and turning black—can be identified inside the battery case, as pictured in Figure A3c. In combination with a sudden temperature increase and pressure pulse, this moment is defined as Thermal Runaway of the triggered cell (④). As pictured in Figure A3c, this pressure pulse is accompanied by a significant gas and smoke leakage that is also measured outside the battery case by the mobile gas-sensing unit. The concentration of gases was higher than the recommended human exposure, triggering the intern warning. Please note that the detection of gases inside the passenger cabin is one criteria for passing the GTR Thermal Propagation test [24]. It has to be mentioned that no flames were visible at this time due to the absence of an ignition source and displacement of oxygen by the released gases inside the battery case. This changed when either the sealing or the polycarbonate lid was thermally damaged, as shown in Figure A3d in Appendix A.

Comparing the described Test A with the remaining tests, using the characteristics given in Table 4, the repeatability of the test setup is evaluated. With the exception of the highlighted readings, a very high concordance of both timings and temperatures between Tests A and B as well as C and D is observable. However, a greater difference between Tests C and D is recognisable as all events of Test D were slightly delayed. Since the accidental limitation of the charging current by factor 10 caused reduced ohmic losses by $\approx 1/100$ (see Equation (2)), the internal heat generation of the cell was reduced in Test D—thus, the observed delay is reasonable. Despite these variations, the experiments are considered to be identical due to the achieved maximal variations of approximately 120 s, the main development is unaltered and the characteristic events are consistent even under the various influences, e.g., heat transfer resistances between heater and cell. Thus, in the following, only figures of Test A are given and key characteristics of the other test are listed in a tabular form.

3.2. Sensor Readings

The additional sensor readings of Test A are presented in Figure 4, relative to the same four characteristic events mentioned above. Please note the significant pressure impulse used for defining ③, while all graphs represent raw data by the sensors, the pressure was filtered by a moving median filter with window-size 10 to decrease the noise. As mentioned above, the utilised air quality sensor returns both raw measurement data and an internal calculated air quality index. During the startup, this index is zeroed based on the current environmental conditions and 100 was defined as the baseline, as indicated in Figure 4. The readings were then mapped to an interval of [0;500]. Due to this integrated self-compensation of environmental influences, this index seems much more suitable for both fault detection and comparison in between tests than the raw data—especially, since sudden change in gas concentration relative to the normal operation are more of interest than the actual concentration.

For better comparability between sensors and tests, the readings from the smoke and strain sensors were standardised each by a subtraction of the average reading at the start up. Thus, the baseline for a normal operation is set at 0, as shown in the corresponding graphs.

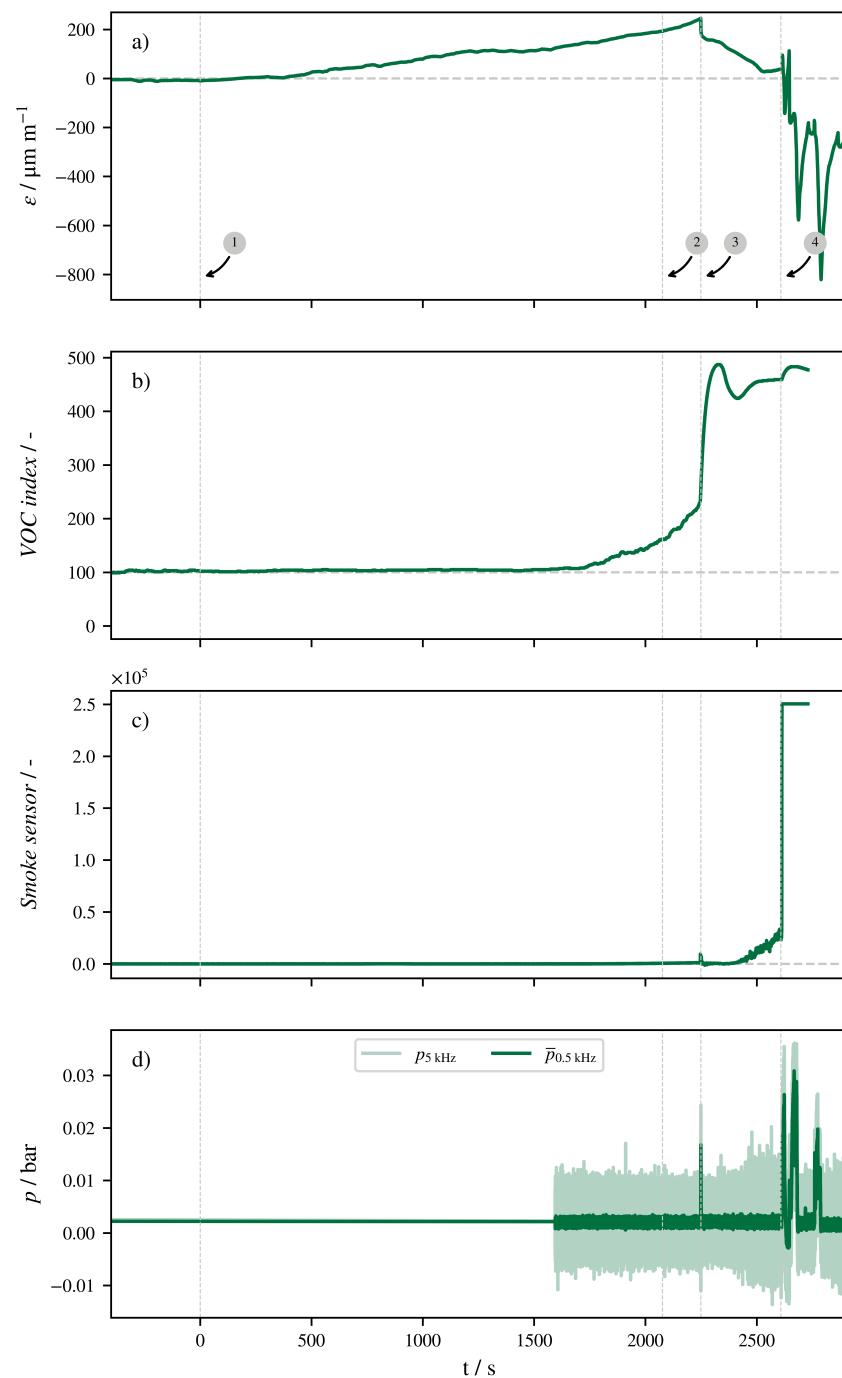


Figure 4. Development of sensor reading during thermal triggered Thermal Runaway for test A (5 K min^{-1}). ① Start of heating. ② Activation of OSD-device. ③ Rupture of burst-disc. ④ Thermal Runaway. (a) Strain of module, (b) index for presence of VOC, (c) infrared-based smoke sensor, (d) over-pressure of battery case; raw signal and filtered by moving average filter.

3.2.1. Strain Sensor

With the start of the heating, the continuous growth of the strain reading is observable, which is reasonable as the increasing temperature causes both thermal expansion and internal gas generation (see Table 1) of the cells. Please refer to Figure 5 for a more detailed display of the data. Here, a subtle plateau can be identified at 1000 s to 1500 s before the reading drops significantly after ③. This behaviour is in accordance with the hypothesis of gas generation inside the battery as this pressure is released with the opening of the burst-disc.

The strain immediately increased with the start of the heating—that is, before gas generation is plausible. Therefore, a superimposed effect by the thermal expansion of the heating device is suspected. However, due to the relaxation of the strain towards the initial baseline after the rupture of the cell—and release of internal pressure—the cell pressure is most likely contributing to the increasing strain as well. This is also confirmed by the complete stress relief after the Thermal Runaway of the cell—please note the chronological correspondence to the pressure pulses at the bottom of the Figure.

During the period between ① and ③, a difference $\Delta\epsilon$ of approximately $255 \mu\text{m m}^{-1}$ was observed. Please find the values corresponding to the other tests in Table 5. Over three tests, the burst-disc ruptured consistently at approximately $215 \mu\text{m m}^{-1}$ to $260 \mu\text{m m}^{-1}$. In contrast, the strain sensor of Test D has not measured any significant positive strain. Due to the high accordance of the other tests, either a sensor malfunction or a fault of the glued connection is suspected.

Table 5. Module strain difference between start of heating ① and rupture of burst-disc ③ during external heating with 5 K min^{-1} (A,B) and 8 K min^{-1} (C,D). Potential measurement error marked in red.

	A	B	C	D
$\Delta\epsilon$	$255.16 \mu\text{m m}^{-1}$	$215.91 \mu\text{m m}^{-1}$	$259.33 \mu\text{m m}^{-1}$	$66.85 \mu\text{m m}^{-1}$

The observed behaviour differs significantly from the reference test without the external heating mentioned above, as investigated separately in Figure 5 relative to the module SOC. Under normal conditions, a positive correlation between ϵ and SOC is identified. Thus, at 300 s or 1400 s, the strain value drops as SOC drops. This behaviour is in good accordance to previous investigations, such as [44], as the ions change the structure and dimension of the active material during the intercalation. The correlation with the changes of SOC is also found within the above-mentioned plateau at 1000 s to 1500 s in Figure 4. Here, the thermally induced expansion of the module is counteracted by the shrinking caused by the period of large discharge in the dynamic profile at this moment.

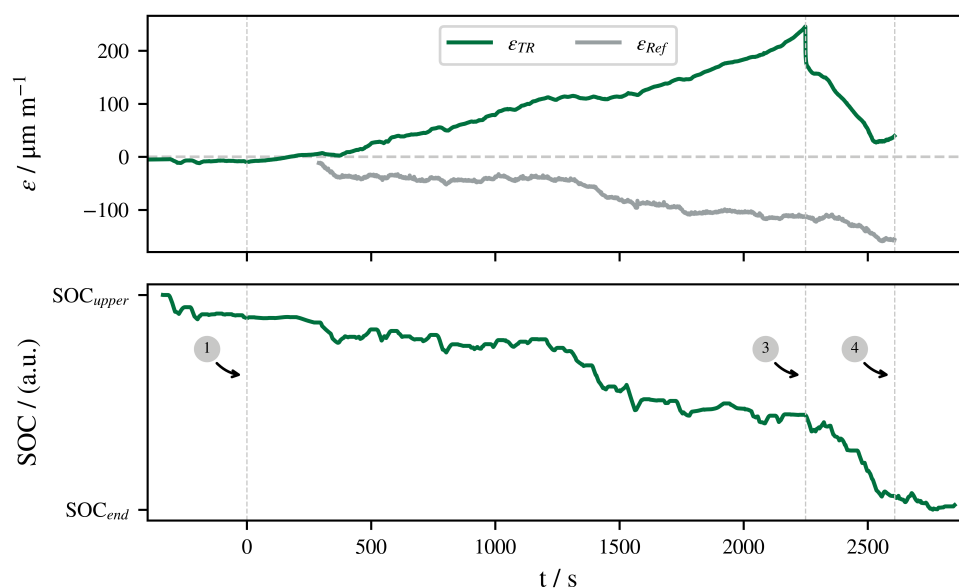


Figure 5. Development of module strain during external heating with 5 K min^{-1} ϵ_{TR} in comparison to reference dynamic profile ϵ_{Ref} (see Section 2.2) and SOC. Characteristic events: ① start of heating, ③ rupture of burst-disc and ④ Thermal Runaway.

3.2.2. VOC Sensor

The air quality index left the baseline a significant time before ②. Since the cell should be still encapsulated at this moment, the cause for this measurement is suspected to stem from outside the cell, e.g., smouldering of plastic module parts or components of thermal or electrical isolation. Since T_{Heater} has already reached temperatures above 200 °C at this moment, this seems plausible. However, this clear pre-② behaviour cannot be identified for the remaining three tests. As the other tests are very comparable based on the other signals described above, the pictured phenomenon is most likely not characteristic for the Thermal Runaway behaviour and arbitrarily caused by the smouldering external test equipment. For the other tests, a slight increase is detectable post-②—also most likely caused by smouldering plastic parts. With the opening of the burst-disc ③ and subsequent smoke release, a significant peak is visible, reaching almost the sensor-range limit. As the burst-disc rupture is accompanied by smoke, inter alia, from electrolyte evaporation containing H_2 and C_xH_y , this behaviour is highly expected. For the remaining duration until Thermal Runaway, only a small recovery is observed.

During a normal operation, it is expected that the gas concentration within the module does not fluctuate so much, especially as the module is encapsulated in the battery case and the vehicle. Thus, the influence of external conditions is considered low. Measuring 45 min within the test environment supports the hypothesis, as approximately constant values within 102.71 ± 2.04 as $1-\sigma$ interval were measured. Thus, the observed behaviour during abuse differs significantly from the readings in the normal operation.

3.2.3. Smoke Sensor

Within all four tests, the readings from the smoke sensor first showed significant deviation from the baseline, with the opening of the burst-disc ③ and an increase continuously until the cell failed thermally ④. The latter event is indicated by a significant peak up to the full measurement range. However, due to the extreme nature of Thermal Runaway, it cannot be determined whether this is a reasonable reading or caused by a thermal destruction of the sensor. As discussed above, event ③ is accompanied by smoke-release, causing accumulating particles inside the module case, providing a reasonable explanation for the behaviour. Similar to the VOC-sensor, small values—hidden by the large range—were already measured before the cell opened. This effect is in accordance to the smouldering suspected above, caused by the high temperatures of the heater and CO1 at this period.

Within the same reference measurement as the VOC-sensor, highly constant behaviour was identified as well, with a $1-\sigma$ interval of -14 ± 32 .

3.2.4. Pressure Sensor

As mentioned in Section 2.2, the pressure measurement was delayed due to the size of the measurement data. While the signal is significantly effected by the measurement noise, the rupture of the burst-disc and release of built-up internal over-pressure can be clearly identified—synchronous with readings from VOC and smoke sensors. The later Thermal Runaway is also accompanied by significant pressure-shocks greater than the first one. This behaviour is additionally observed with all four tests. Please note that the deviation from the values reported in previous studies (see Section 1, Table 1) were significantly greater than the findings in these tests. Two causes were identified for this deviation:

1. Reduction in the pressure by the dead volume within the mainly empty battery case.
2. Leaks in the sealing of lid and cable bushings.

The later cause is indicated by significant gas concentrations outside the battery case measured by the mobile-gas-sensing unit, synchronous with pressure peaks. This leakage is also visible in Figure A3c) in Appendix A. Thus, under standard conditions in the application, e.g., more modules and proper cable bushings, larger pressure-shocks have to be expected unless an over-pressure valve/relieve is provided for this range.

Obviously, under a normal operation, the signal of such a relative pressure sensor is mainly influenced by the measurement noise, as indicated by small and constant values before ③. Thus, the signal from the pressure sensor differs from normal behaviour as well.

3.3. Approaches for Early Fault Detection

In the previous sections, it was found that the appearance of a thermal fault is indicated by all utilised quantities as the behaviour during abuse significantly differs from reference measurements. This observation is in high accordance to experiments on lab-level referenced in the introduction and similar previous work [67]. In addition to the aforementioned usage in describing the process of the Thermal Runaway, the feasibility for early fault detection should be discussed in the following sections.

Based on the raw strain measurement displayed in Figure 5, detection seems possible approximately immediately with the start of heating. However, as the systematic measurement deviation by the experimental setup itself—as discussed above—cannot be reasonably corrected, any detection result would be biased. Therefore, the strain measurement is excluded from further investigation. However, the clear positive correlation between ϵ and SOC, shown in Figure 5, suggests a great approach for temperature monitoring that has to be investigated further with a more robust experimental setup. Since the feasibility of detection based on temperature measurement highly depends on the position of the sensor relative to the triggered cell (see Figure 3) and the large deviation between T_{01} and T_{12} or T_{mean} , it is also excluded from the analysis.

In Figure 6, the measured voltage is given together with the reference signal generated by the employed model. As discussed in Section 2.2.2, one model is used as reference for every cell. The deviation between model output and measurement can be identified in the top subplot but becomes more obvious within when comparing the residuum of the cells U_{01} and U_{12} , as pictured in the lower subplot. Due to the experimental setup of heating C01, C12 is approximately still within normal operation conditions, resulting in a smaller residuum $\Delta U_{Sim-C12}$. With continuous heating, the difference $\Delta U_{Sim-C01}$ approaches the lower threshold (-20 mV, as indicated in Figure by a red horizontal line). However, the first surpass, approximately at 450 s, does not trigger a warning as the second condition of $t \geq 0.5$ s is not met. The usefulness of the implemented timing condition can be seen approximately at 1700 s where an irregularity in both residua is observed. Due to the very dynamic characteristic, a faulty reading is suspected—either the cell voltage or the load current. However, this event would not have triggered a fault-positive warning due to the threshold design. Further in the test, this condition is exceeded and a fault detection is presumed—significantly before ②. The same results were achieved for the other tests, as summarised in Table A1 in Appendix A. Thus, the proof-of-concept described initially in [68] has been successfully transferred from cell level to module level, and the feasibility has been confirmed. As the achieved detection time is highly dependent on the chosen thresholds, the selection of these provides an approach to increase the pre-warning time. In the scope of this work, the thresholds were defined based on the measurement-model-deviation under normal conditions. Therefore, improving the overall model accuracy would be necessary. In this context, a feedback loop of observation, e.g., as incorporated in Kalman Filters, would provide a long-term stable simulation as offsets would be corrected. However, such Kalman Filter would also correct the fault-offset; because of this, combined approaches such as [79] seem reasonable. Defining adaptive thresholds, e.g., dependent on the ambient temperature based on an extensive statistical analysis of the model and module behaviour under different operational boundaries, is another approach for narrower detection limits. In addition, the pictured deviation between U_{01} and the remaining cells, as shown in Figure 3, can also be evaluated by methods other than model-based ones. However, these often referenced as *signal-based* [80] methods are outside the scope of this paper.

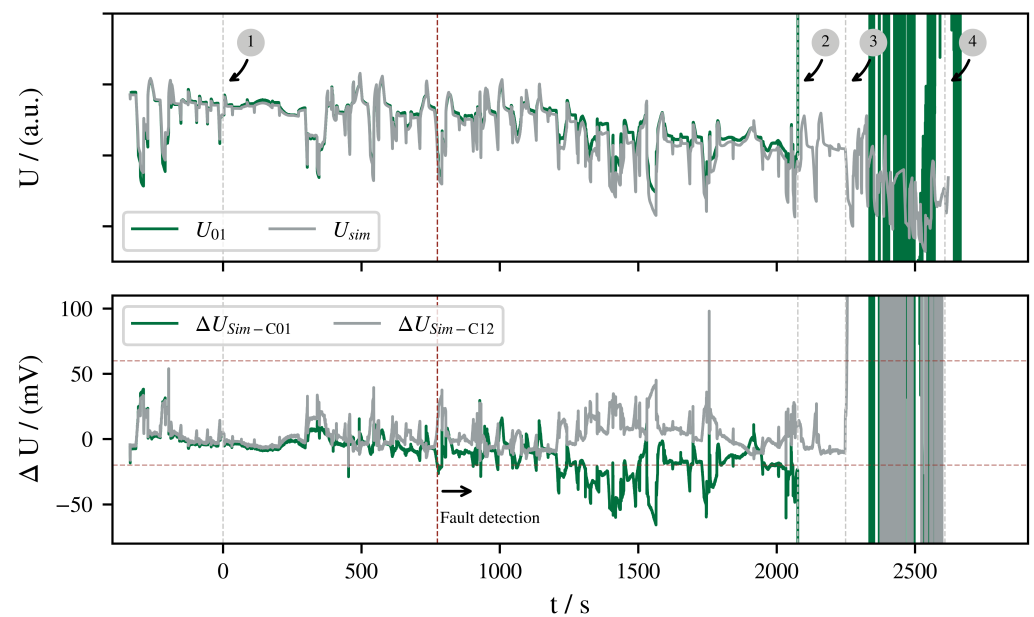


Figure 6. Model-based detection of external heating in Test A. Measured and simulated voltage of C01 (top); model deviation from C01 and C12 as fault signal (bottom). Characteristic events: ① start of heating, ② Activation of OSD-device, ③ rupture of burst-disc and ④ Thermal Runaway.

With the presented test setup, the method was only validated against thermal faults. The faults of internal short circuits, however, were not experimentally investigated since the application of such a trigger would have required a significant modification of the battery module. Nevertheless, these faults are considered to pose a serious risk [81,82], especially due to the spontaneous development and the little options for control from the outside [83]. It is known that the practical faults caused by impurities or dendrites show characteristic fusing phenomena [84], describing the behaviour of a short voltage drop that recovers quickly when the point of contact melts due to resistive heating [39,84]. This short voltage drop is often greater than the threshold chosen in Section 2.2.2 and develops into a safety-critical hard short circuit over time [15,85]. Thus, it is expected that the method presented detects such internal short circuits with a significant voltage drop as well. In the literature, a common test setup for representing internal short circuits is a sudden voltage drop of $\Delta U \geq 0.1 \text{ V}$ [13,54]. Since this voltage deviation is greater than the threshold from Section 2.2.2, the method can pass these tests as well. Long-term high-ohmic short circuits lead to a slow deviation of the SOC and OCV [86]. In addition, it depends on the implemented balancing strategies whether and how fast this trend can be identified by the model.

As the modelling approach requires determination of the model parameters and verification of the model, the achieved result is compared to multiple, more simple sensor-based detection methods. Although there are various methods from data science or statistics for evaluating the measured quantities, a quite rudimentary approach based on pre-defined thresholds was chosen for the scope of this paper, as summarised in Table 6.

Using these detection approaches, the pre-discussed data of the abuse Tests A, B, C and D were evaluated. Here, the first threshold-exceeding is considered as the time of detection. The method-dependent results for each test are summarised in Figure 7 in comparison to the four characteristic events that are repeatably addressed. Please also note the above-mentioned 5 min pre-warning time required by the GTR [24] indicated in dashed-red relative to ④ of each test. The achieved detection times and corresponding temperatures T_{01} and T_{12} are listed within Appendix A in Table A1.

Table 6. Evaluation methods for detection of thermal fault. Thresholds defined by lower cut-off voltage U_{min} and by reference measurement (see Section 3.2). $\bar{x}^{(t)}$ represent a moving average with window size t .

Index	Quantity	Evaluation
I	Voltage	$U_i \leq U_{min}$
II	Voltage	Model residuum (see Section 2.2.2)
III	Gas	$\overline{VOC}^{(10s)} \geq \overline{VOC}_{ref} + 5 \cdot \sigma_{VOC}$
IV	Smoke	$\overline{IR}^{(10s)} \geq \overline{IR}_{ref} + 5 \cdot \sigma_{IR}$
V	Pressure	$\bar{p}^{(2ms)} \geq 0.01 \text{ bar}$

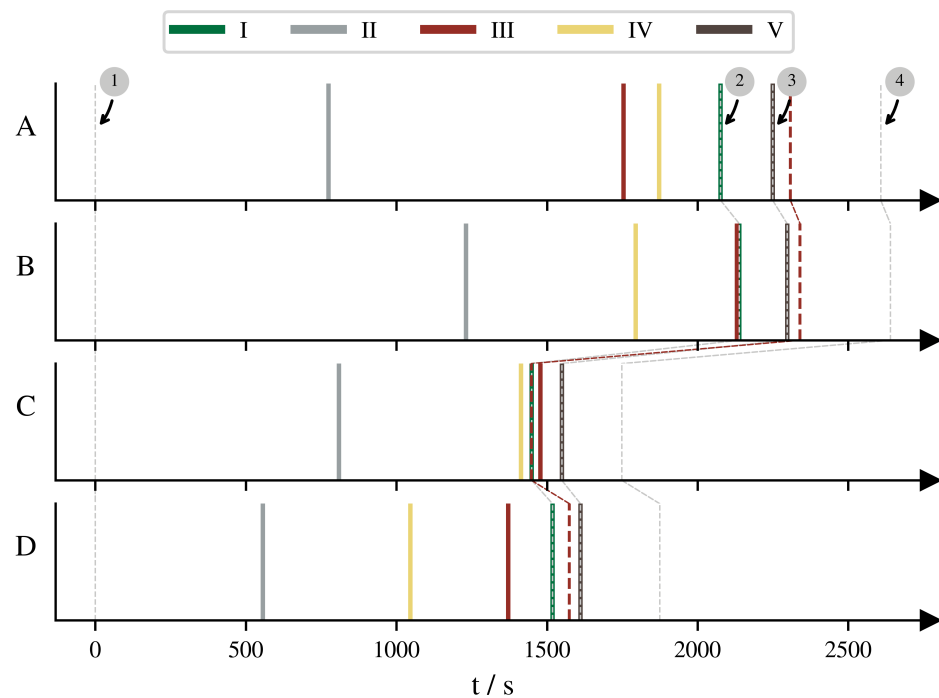


Figure 7. Time map of sensor-based fault detection relative to the start of heating and pre-warning to Thermal Runaway (4) triggered by external heating with 5 K min^{-1} (A,B) and 8 K min^{-1} (C,D). Please find method description in Table 6. Characteristic events 1 Start of heating, 2 Activation of OSD-device and 3 Rupture of burst-disc are marked by grey dashed lines. The GTR-5 min-criteria is marked by a red dashed line.

With all given detection approaches, the thermal abuse of the module can be identified before Thermal Runaway of C01; however, the achieved pre-warning times differ slightly in between tests and significantly in between signals. The fact that detection times vary between tests despite a deterministic definition and almost identical key characteristics (see Table 4) underlines the importance of multiple reruns of abuse tests for reliable results.

Within the presented tests, the model-based approach is identified as the fastest method over all four tests compared to the different sensor-based methods investigated and—with the exception of Test B—quite constant with regard to the detection time as well. It has to be underlined that the warning of the model-based method (II, grey line) is significantly earlier when compared to the other sensor-based approaches. In contrast, the pressure-based detection (V) recognised the existing fault always last. However, with the tests at a lower heating rate (A, B), the pressure signal still fulfils the GTR criteria due to the duration between 3 and 4. In addition, this criteria is achieved for each setup by all other sensors with the exception of the voltage threshold (I) and VOC (III) in Test C, in which detection is delayed by 130 s and 330 s, respectively. Since it is unclear whether a correct

charging power in Test D would have accelerated the events, sensor-based detection of faults might become difficult with higher heating rates.

Thus, dependent on the desired pre-warning time, all detection approaches can be utilised. This finding is also in accordance to the results from Koch et al. [67]. As the sensor-based methods require an opening of the cell or at least smouldering of adjacent components, detection is only possible relatively far into the process of Thermal Runaway. In contrast, the model-based approach utilises inherent information on the cell temperature from the dynamic behaviour and, therefore, detects the external heating early. Since the detection based on smoke and air quality even before the opening of the cell is caused by smouldering of components outside of the battery, the general feasibility is questionable. On the one hand, the origin of the detected smoke and gases is unknown and eventually caused by the manipulation of the original module; on the other hand, even unaltered modules have various flame- and smoulder-able components. Thus, in comparison to the pressure sensor, both sensors provide the opportunity to detect fault-induced heating either before the cell-opening by smouldering or approximately synchronous with the opening by the vaporised electrolyte. This sensitivity to multiple failure cases is also underlined in [87].

In previous works such as [67,88,89], the authors have rated detection methods based on criteria additional to the warning time itself. These criteria are summarised analogously in Table 7 and the methods are discussed before roughly evaluated.

Table 7. Evaluation of the detection methods, taking into account the detectability as well as the possibilities for integration into application-oriented battery systems on the basis of relevant criteria from previous research. Rating scale ranges from positive (+) over neutral (o) to negative (-).

Method	$t_{Detection}$	Certainty	Localisation	Monitoring	Complexity	Integration	Scalability	Transferability
Voltage threshold	-	+	+	+	+	+	o	o
Model-based	+	+/-	+	+	-	+	+	+
Cell temperature ¹	+	-	-	+	-	+	-	+
Strain ²	+/o	o	o	o	+	o/-	o/-	+
Gas	o	+	o	-	+	o	+	+
Smoke	o	+	o	-	+	o	+	+
Pressure	-	+	-	-	o	-	+	+

¹ Assumption: temperature sensors at cell level available. ² Please refer to Section 3.2.1 for limitations.

Besides the warning time itself, the certainty of the generated fault signal was adopted from Koch et al. [67], representing the shape of fault signal where a step function is considered as optimum. As presented in Figure 4, the ambient sensors provide such behaviour as well as the voltage due to the OSD. In this context, the simple sensor setup with approximately binary output signals has the advantage that evaluation of the signal concerning the actual battery state is not complex. However, on the other hand the sensor setup is not capable to differentiate the severity of the current battery state. Thus, smouldering caused by a faulty chip (low severity) will cause the same fault signal as extensive venting of electrolyte (high severity). Here, either the combination with other sensors, e.g., pressure, might be advantageous or the implementation of a more advanced smoke sensor that provides more insights like smoke density or a high sensitivity at certain particles characteristic for Thermal Runaway. For the latter variant, however, a deep knowledge of the module emissions during failure is required—potentially even at various states of health. The model-based method output, however, depends on whether the refined detection threshold with a clear moment of detection is used or the generated fault signal $\Delta U_{Sim-C01}$ is used that is less certain. Because of this signal spread, the fault detection by temperature differences is also considered to be a method of low certainty.

As fault location or fault isolation is a recurring aspect with fault detection, e.g., [90], meaning the identification of the faulty cell within the whole system, this is evaluated as well. Obviously, the methods on cell level provide such functionality while the system-based sensors, e.g., pressure, cannot. In a similar way, the external system-located envi-

ronmental sensors are not well suited for evaluating the current cell or rather battery state. In contrast, the generated fault signal by model or temperature sensor as well as voltage monitoring can indicate the state, e.g., actual SOC, as usually performed by the BMS.

From an application-based viewpoint, the complexity is an important criterion that evaluates the effort for incorporating the method into a battery system. Both model and cell temperatures are rated with high complexity, as they require significant work for validation and parameterisation or sensor topology, respectively. However, most manufacturers or OEMs already have detailed insights into the battery characteristics dependent on various parameters like SOC, temperature, operation and SOH. Therefore, the effort for model parameterisation might be reduced in reality. The pressure sensor was rated moderate since it requires modification of the battery case for the implementation of the sensor and gas-tight sealing. Furthermore, the logging of the high-frequency data might become challenging.

The incorporation of the methods described into a battery system is evaluated by the integration criteria, where voltage, model and the integrated-circuit-based environmental sensors are suited best and good, respectively, since the quantities are either already utilised in application or easy to implement due to the internally pre-calculated digital output. In contrast, the cell-based temperature measurement increases the required data acquisition relative to the actual common configuration with one or only few temperature measurement locations (see Figure 1). As the strain sensor has only worked in three of four cases, the general evaluation is not clear. The high sample rate for pressure monitoring also requires further effort for integration; however, as the chosen sample rate was based on former experimental experience, there could be possibilities for optimisation. Based on the observed pulse duration in this configuration of approximately 2 s, a smaller sample rate might be feasible as well. Furthermore, long-term storage of high-frequency data is not needed.

From an application-based viewpoint, scalability is a critical aspect since a battery case as investigated holds eight individual modules in series connection that have to be monitored during operation. As VOC, smoke and pressure were already measured at battery case level (see Table 2), no adjustments have to be made to monitor multiple modules—these methods are rated with great scalability. Due to the assumptions made when designing the model, every cell is considered equal. Thus, the model just has to be calculated for one reference cell and the output compared to each individual cell voltage. Assuming that cell-level voltage monitoring is already required for other monitoring functions, e.g., cut-off voltages or SOC tracking, besides calculation of $U_{Sim} - U_i$ no additional effort has to be made. Thus, the model-based approach is considered to be well scalable. For the same reason the hard voltage threshold (I) is rated with moderate scalability. With reference to Table 2, strain was measured on module-level. Therefore, an additional sensor is needed for each module in such a battery case. As this is considered to be more complex and costly than just calculation, the scalability is rated below the model-based approach. It has to be mentioned that this evaluation is based on the assumption of a module made from prismatic or pouch cells mounted compactly. The implementation of such a module-level measurement topology on a module consisting of cylindrical cells can be difficult or even impossible. Due to this restriction, there is a high dependence on the scalability of the module and cell design.

Within this study, only one cell chemistry was investigated; thus, the transferability to other cell types has to be evaluated as well. As discussed above, the clear failure indication by the cell voltage was caused by the implemented OSD and, therefore, the feasibility is mainly independent of the chemistry or cell size but dependent on the safety measures by the manufacturer. However, the available safety devices and their behaviour during different failure mechanisms have to be known in detail. Since this information is not accessible for a regular customer in general, the transferability is rated neutral. The proposed model-based approach utilises the temperature dependent change of impedance and the slightly influenced open-circuit voltage of the considered cell. This parameter dependency

is caused by the temperature influence on the reaction rate of the electrochemical processes and valid in general. Hence, a similar failure characteristic is expected with all cathode compositions such as NMC as well as with LFP, LTO, etc. Please refer to Klink et al. [68] for a brief comparison of cell impedance with variable shape and size as well to [31]. Therefore, the transferability is considered as very good, especially since the same method was already successfully implemented previously on another cell type. In a similar way, it is expected to recognise cell faults by monitoring the cell temperature independent on the cell type or chemistry. This can be caused either by decomposition reactions as well as by ohmic heating in the case of internal or external short circuits. However, the location of the temperature sensor relative to the fault location has a large influence on the achievable sensitivity as indicated by simulations from Feng et al. [91]. Therefore, good transferability is considered and mechanical properties such as the size and the thermal mass as well as the available heat transfer paths are identified as most relevant for the sensitivity. Safety measures like passive cooling systems will delay temperature-based detection since they smooth thermal inhomogeneities [20]. As mentioned in Table 1, internal pressure is built up during heating due to thermal expansion and electrolyte evaporation. As before, these processes are mainly independent of the selected cell; therefore, thermal failure is expected to cause mechanical stress over different cell types and sizes. However, the implementation of strain measurement might be difficult with alternating types such as pouch bags. Following the above-mentioned reasoning in combination with Table 1, the transferability of gas, smoke and pressure is rated with good since the evaporation of electrolyte is expected with all cells. With exception of the smouldering, all three sensor types require the opening of the cell, therefore, the availability of over-pressure safety devices as well as the mechanical stability of the cell casing influence the achievable time of detection.

Consequently, based on the requirements of detection time and additional complexity, battery monitoring can be extended by one or a combination of the investigated sensors. By combining multiple methods, fault-positive signals from one method can be identified and trigger-thresholds set more broadly to deal with disturbing factors in practice. This approach can be also found in recent works but limited to voltage or temperature readings [92].

4. Conclusions

Based on the state of knowledge of the Thermal Runaway process of lithium-ion batteries, a multi-sensor monitoring setup was designed within the boundaries of a battery case from automotive application. By means of a brief literature review, the main principles of the individual fault signals were presented and ranked concerning the approximate temperature ranges. The sensor setup was experimentally validated by Thermal Runaway tests triggered by an external heating device using 5 K min^{-1} and 8 K min^{-1} in two repetitions each.

It was found that, despite criticisms of the repeatability of the abuse tests, the development of Thermal Runaway was highly constant based on activation of OSD, rupture of burst-disc and the Thermal Runaway itself. Within all sensor readings, a deviation in the reference behaviour or baseline was identified and discussed. With the exception of the strain measurement that was affected by the test setup all readings were found to be reasonable and suitable for further evaluation in a threshold-based thermal fault detection approach. For comparability the results are set into contrast with a model-based approach and the 5 min-requirement by GTR.

All sensors were capable of identifying the thermal fault before Thermal Runaway; however, especially with the slow heating rate, the model-based approach was by far the fastest. Based on the known behaviour of internal short circuits, the feasibility for this fault was discussed as well and positively evaluated. Dependent on the existence of smouldering both smoke and VOC sensing registered the thermal fault even before opening of the cell, at which moment the fault is detected by the the pressure-based method.

Based on the identified detection times and, for example, requirements for up-scaling, the model-based approach is the most convincing but the other methods are suitable as well as compared in Table 7—at least as simple-to-implement redundant monitoring for low false-positive rates. This result is further considered as transferable to other cells and cell types with limitations due to mechanical design and implemented safety devices.

However, for implementing the model-based approach in application, a solution is still required for the problem of dealing with ageing-induced parameter changes for long-term functionality, as predicting ageing was outside of the scope of this paper. In addition, a detailed evaluation of the identified increasing voltage deviation in between cells with the methods other than the presented model-based approach seems promising and has to be investigated in future work.

Author Contributions: Conceptualisation, J.K., J.G. and A.H.; methodology, J.K. and A.H.; software, A.H.; validation, A.H., N.O., J.G. and J.K.; formal analysis, J.K. and A.H.; investigation, J.K., A.H., N.O. and J.G.; resources, U.N.; data curation, J.K. and A.H.; writing—original draft preparation, J.K.; writing—review and editing, J.K., J.G., A.H. and U.N.; visualisation, J.K.; supervision, R.B. and H.-P.B.; project administration, U.N. and R.B.; funding acquisition, U.N. and R.B. All authors have read and agreed to the published version of the manuscript.

Funding: Parts of this research were founded by the Federal Ministry for Economic Affairs and Energy of Germany in the project RiskBatt (project number 03E13010A).

Institutional Review Board Statement: Not applicable.

Informed Consent Statement: Not applicable.

Data Availability Statement: The data presented in this study is available on request from the corresponding author.

Acknowledgments: We thank Scania CV AB for providing battery modules and battery cases enabling tests close to application as well as the support in data, organisation and preparation of the extensive experiments. In addition, we thank Draeger Safety AG & Co. KGaA for providing the mobile gas-sensing unit. For conducting the high-energetic abuse tests we are grateful for having had the opportunity to switch to a test field of VoltaLabs, Goslar. The authors acknowledge the financial support by the Federal Ministry for Economic Affairs and Energy of Germany in the project RiskBatt (project number 03E13010A). We acknowledge support by Open Access Publishing Fund of Clausthal University of Technology.

Conflicts of Interest: The authors declare no conflict of interest. The founders had no role in the design of the study; in the collection, analyses, or interpretation of data; in the writing of the manuscript, or in the decision to publish the results.

Abbreviations

The following abbreviations are used in this manuscript:

BEV	Battery Electric Vehicle
BMS	Battery Management System
CC	Constant Current
CID	Current Interrupt Device
CMC	Cell Management Controller
CV	Constant Voltage
DUT	Device Under Test
GTR-(EVS)	Global Technical Regulation (on Electrical Vehicle Safety)
IR	Infra Red
LFP	Lithium-Iron-Phosphate
LTO	Lithium-Titanium-Oxide
NMC	Nickel-Manganese-Cobalt
OCV	Open Circuit Voltage

OEM	Original Equipment Manufacturer
OSD	Over-charge Safety Device
PHEV	Plug-In Hybrid Electric Vehicle
PID	Proportional-Integral-Derivative Controller
SEI	Solid Electrolyte Interface
SOC	State of Charge
SOH	State of Health
VOC	Volatile Organic Compound
WHVC	World Harmonised Vehicle Cycle

Appendix A

Appendix A.1. Model-Based Fault Detection

Figure A1 pictures the schematic of the two-layered model, coupling electrical and thermal processes, as described in detail in [68]. The main purpose of the model—as pictured—is providing a reference value for evaluating the measured cell voltages during operation. With later application on a BMS in mind, a simplified approach based on equivalent circuit models (ECM) was chosen. As proven in various previous studies (e.g., [93]) this setup provides adequate accuracy for the comparison without the computational expense of spatially resolved differential equations.

Due to the serial connection of cells every cell has the same load current and following Equation (2) the same heat generation. In combination with the assumption of a simplified heat transfer path from the active material to the cooling fluid in the bottom plate that is identical for each cell as well, all cells have the same thermal characteristic. Quality assessment of the module under investigation has further found, that the cell parameters are so close to each other that no difference can be identified between individual cells. Thus, modelling the thermal behaviour of just one cell is sufficient for describing the full module. With this assumption calculating just one electrical model is sufficient as well since—in addition to the temperature—the current and SOC are also identical due to the series connection.

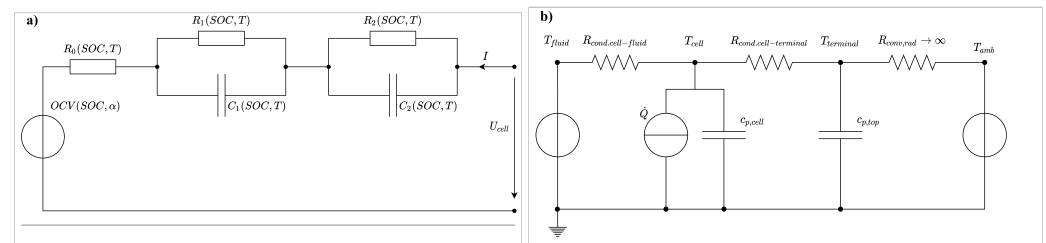


Figure A1. Structure of the equivalent circuit models (ECM). (a) Electrical ECM for modelling the cell voltage U_{cell} under the influence of the load current I . Both the parameters and the voltage source OCV were implemented as look-up tables based on data samples gathered beforehand. (b) Thermal ECM for tracking the cell temperature during load and with heat dissipation to the cooling fluid. Besides the cell temperature T_{cell} that is used to update the model parameters in the electrical model $T_{terminal}$ is modelled, representing the position of the temperature sensors. Heat dissipation by convection or radiation towards the ambient was neglected.

Based on the model-design described above the model-based fault detection is implemented as pictured within the flowchart in Figure A2.

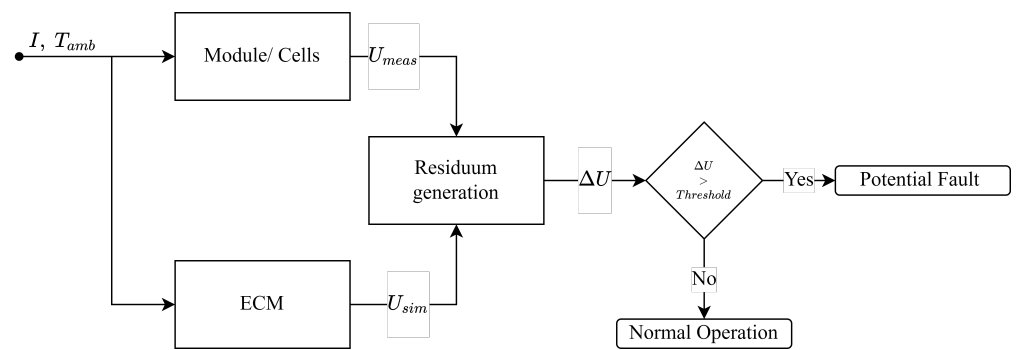


Figure A2. Structure of the implemented model-based fault detection as initially presented in [68]. For details on residuum assessment please refer to Section 2.2.2.

Appendix A.2. Results

The development of the thermally triggered failure of the battery module is documented by the screenshots presented in Figure A3. While the rupture of the burst-disc is only slightly indicated by small amounts of white smoke in Figure A3b the massive smoke generation during Thermal Runaway can be identified in Figure A3c. In addition to the corresponding to the characteristic events mentioned before throughout the document, the fast development can be identified by the given timings.

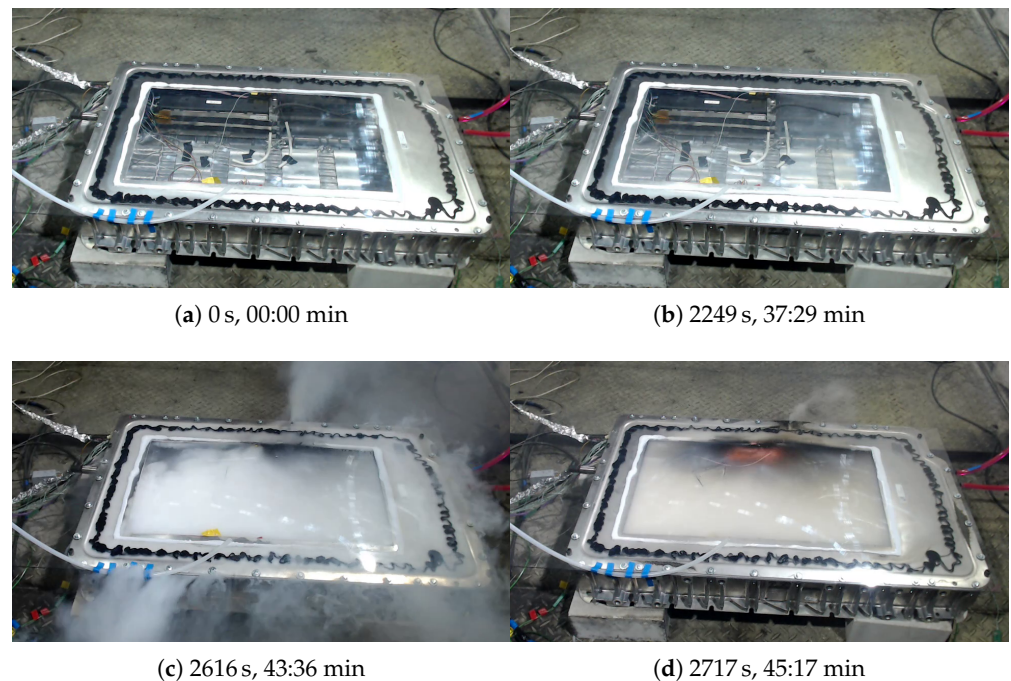


Figure A3. Screenshots of Test A at characteristic events. Small time offsets relative to Table 4 to capture the smoke after the event. (a) Start of heating ①, initial state. (b) Rupture of burst-disc ③, start of slight white smoke release. (c) Thermal Runaway ④, massive white smoke generation and pressure-caused leakage of battery case. Significant upwards leap of T_{01} , see Figure 3. (d) First Flames, ignition and black combustion products at crack in sealing.

In addition to the time map of the individual detection methods given in Figure 7 a summary of the detection times is displayed for all four test within Table A1. Besides the detection times and pre-warning duration Δt_{TR} the cell temperatures of the first and last cell are given. Due to the large deviation of the temperatures T_{01} and T_{12} the disadvantage of just one point of temperature measurement in the case of a local fault becomes clear.

Thus, the indirect measurement on cell level by the model-based approach provides more detailed insights.

Table A1. Fault detection time relative to the start of heating and pre-warning to Thermal Runaway (④) triggered by external heating with 5 K min^{-1} (A,B) and 8 K min^{-1} (C,D). Adjacent and most distanced cell temperatures T_{01} and T_{12} given at the moment of detection. Detailed information on detection methods can be found in Table 6.

		A	B	C	D
I	t	2076.00 s	2138.00 s	1449.00 s	1518.00 s
	Δt_{TR}	532.00 s	502.00 s	299.00 s	356.00 s
	T_{01}	121.61 °C	120.75 °C	119.05 °C	123.27 °C
	T_{12}	29.13 °C	29.03 °C	26.95 °C	27.50 °C
II	t	774.00 s	1231.00 s	809.00 s	556.00 s
	Δt_{TR}	1834.00 s	1409.00 s	939.00 s	1318.00 s
	T_{01}	48.73 °C	67.12 °C	62.65 °C	44.53 °C
	T_{12}	26.34 °C	26.48 °C	25.27 °C	25.54 °C
III	t	1754.00 s	2130.00 s	1478.00 s	1371.00 s
	Δt_{TR}	854.00 s	510.00 s	270.00 s	503.00 s
	T_{01}	101.70 °C	120.38 °C	123.04 °C	106.63 °C
	T_{12}	29.29 °C	29.11 °C	27.37 °C	26.72 °C
IV	t	1872.00 s	1794.00 s	1413.00 s	1046.00 s
	Δt_{TR}	736.00 s	846.00 s	335.00 s	828.00 s
	T_{01}	108.01 °C	99.60 °C	114.54 °C	77.84 °C
	T_{12}	28.57 °C	29.06 °C	26.45 °C	26.01 °C
V	t	2249.00 s	2297.00 s	1549.00 s	1611.00 s
	Δt_{TR}	359.00 s	343.00 s	199.00 s	263.00 s
	T_{01}	118.41 °C	132.30 °C	129.47 °C	135.74 °C
	T_{12}	28.64 °C	29.78 °C	27.29 °C	28.80 °C

References

- Yu, A.; Sumangil, M. Top Electric Vehicle Markets Dominate Lithium-Ion Battery Capacity Growth. Available online: <https://www.spglobal.com/marketintelligence/en/news-insights/blog/top-electric-vehicle-markets-dominate-lithium-ion-battery-capacity-growth> (accessed on 10 January 2022).
- Bodine, R.; Brennan, R. Gas vs. Electric Car Fires: 2021 Findings. Available online: <https://www.autoinsuranceez.com/gas-vs-electric-car-fires/> (accessed on 8 February 2022)
- National Transportation Safety Board. *Aircraft Incident Report: Auxiliary Power Unit Battery Fire*; National Transportation Safety Board: Washington DC, USA, 2014.
- Koh, D.J. Samsung Announces Cause of Galaxy Note7 Incidents in Press Conference. 2017. Available online: <https://news.samsung.com/us/Samsung-Electronics-Announces-Cause-of-Galaxy-Note7-Incidents-in-Press-Conference> (accessed on 10 January 2022)
- Meza, E. Several German Cities Halt Use of e-Buses Following Series of Unresolved Cases of Fire. Available online: <https://www.cleanenergywire.org/news/several-german-cities-halt-use-e-buses-following-series-unresolved-cases-fire> (accessed on 10 January 2022)
- Naughton, K.; Yang, Y. GM Recalls All Bolt EVs on Fire Risk; Sees \$1 Billion Cost, 2021. Available online: <https://www.bloomberg.com/news/articles/2021-08-20/gm-to-spend-1-billion-to-recall-all-bolt-evs-due-to-fire-risk> (accessed on 8 February 2022)
- Liaw, B.Y.; Wang, F.; Wei, Y.; Brandt, K.; Schultheiß, J.; Schweizer-Berberich, M.; Dandl, S.; Wöhrle, T.; Lamp, P.; Jeevarajan, A.J.; et al. Managing Safety Risk by Manufacturers. In *Li-Battery Safety*; Garche, J., Brandt, K., Eds.; Electrochemical Power Sources; Elsevier: San Diego, CA, USA, 2019; pp. 267–378. [CrossRef]
- Pfrang, A. *JRC Exploratory Research: Safer Li-Ion Batteries by Preventing Thermal Propagation*; European Commission: Luxembourg, 2018.
- Feng, X.; Zheng, S.; Ren, D.; He, X.; Wang, L.; Cui, H.; Liu, X.; Jin, C.; Zhang, F.; Xu, C.; et al. Investigating the thermal runaway mechanisms of lithium-ion batteries based on thermal analysis database. *Appl. Energy* **2019**, *246*, 53–64. [CrossRef]
- Wang, Q.; Ping, P.; Zhao, X.; Chu, G.; Sun, J.; Chen, C. Thermal runaway caused fire and explosion of lithium ion battery. *J. Power Sources* **2012**, *208*, 210–224. [CrossRef]

11. Börger, A.; Mertens, J.; Wenzl, H. Thermal runaway and thermal runaway propagation in batteries: What do we talk about? *J. Energy Storage* **2019**, *24*, 100649. [[CrossRef](#)]
12. Jens, T.; Karsten, P.; E. Christopher, H.; A. Daphne, F.; Harry, D.; Jürgen, G.; Verena, L.; Xuning, F.; Minggao, O.; Languang, L.; et al. Li-Secondary Battery. In *Li-Battery Safety*; Garche, J., Brandt, K., Eds.; Electrochemical Power Sources; Elsevier: San Diego, CA, USA, 2019; pp. 507–629. [[CrossRef](#)]
13. Li, X.; Wang, Z. A novel fault diagnosis method for lithium-Ion battery packs of electric vehicles. *Measurement* **2018**, *116*, 402–411. [[CrossRef](#)]
14. Gao, S.; Feng, X.; Lu, L.; Ouyang, M.; Ren, D. A Test Approach for Evaluating the Safety Considering Thermal Runaway Propagation within the Battery Pack. *ECS Trans.* **2017**, *77*, 225–236. [[CrossRef](#)]
15. Brodd, R.J. *Batteries for Sustainability*; Springer: New York, NY, USA, 2013. [[CrossRef](#)]
16. Tidblad, A.A.; Edström, K.; Hernández, G.; de Meaza, I.; Landa-Medrano, I.; Jacas Biendicho, J.; Trilla, L.; Buysse, M.; Ierides, M.; Horno, B.P.; et al. Future Material Developments for Electric Vehicle Battery Cells Answering Growing Demands from an End-User Perspective. *Energies* **2021**, *14*, 4223. [[CrossRef](#)]
17. Liu, B.; Jia, Y.; Li, J.; Yin, S.; Yuan, C.; Hu, Z.; Wang, L.; Li, Y.; Xu, J. Safety issues caused by internal short circuits in lithium-ion batteries. *J. Mater. Chem. A* **2018**, *6*, 21475–21484. [[CrossRef](#)]
18. Lopez, C.F.; Jeevarajan, J.A.; Mukherjee, P.P. Experimental Analysis of Thermal Runaway and Propagation in Lithium-Ion Battery Modules. *J. Electrochem. Soc.* **2015**, *162*, A1905–A1915. [[CrossRef](#)]
19. Zhong, G.; Li, H.; Wang, C.; Xu, K.; Wang, Q. Experimental Analysis of Thermal Runaway Propagation Risk within 18650 Lithium-Ion Battery Modules. *J. Electrochem. Soc.* **2018**, *165*, A1925–A1934. [[CrossRef](#)]
20. Chen, F.; Huang, R.; Wang, C.; Yu, X.; Liu, H.; Wu, Q.; Qian, K.; Bhagat, R. Air and PCM cooling for battery thermal management considering battery cycle life. *Appl. Therm. Eng.* **2020**, 173. [[CrossRef](#)]
21. Kim, G.-H.; Pesaran, A. Presented at the Analysis of Heat Dissipation in Li-Ion Cells & Modules for Modeling of Thermal Runaway (Presentation), Long Beach, CA, USA, 15 May 2007.
22. Darcy, E. Presented at the Driving Factors for Mitigating Cell Thermal Runaway Propagation and Arresting Flames in High Performing Li-Ion Battery Designs (Presentaion), Santa Rosa, CA, USA, 1 May 2015.
23. Doughty, D.H.; Pesaran, A.A. *Vehicle Battery Safety Roadmap Guidance*; National Renewable Energy Lab. (NREL): Golden, CO, USA, 2012. [[CrossRef](#)]
24. UN Global Technical Regulation. Global Technical Regulation No. 20: Global Technical Regulation on the Electrical Vehicle Safety (EVS). Available online: <https://unece.org/fileadmin/DAM/trans/main/wp29/wp29wgs/wp29gen/wp29registry/ECE-TRANS-180a20app1e.pdf> (accessed on 10 January 2022)
25. Yuan, L.; Dubaniewicz, T.; Zlochower, I.; Thomas, R.; Rayyan, N. Experimental study on thermal runaway and vented gases of lithium-ion cells. *Process Saf. Environ. Prot.* **2020**, *144*, 186–192. [[CrossRef](#)]
26. Essl, C.; Golubkov, A.W.; Gasser, E.; Nachtnebel, M.; Zankel, A.; Ewert, E.; Fuchs, A. Comprehensive Hazard Analysis of Failing Automotive Lithium-Ion Batteries in Overttemperature Experiments. *Batteries* **2020**, *6*, 30. [[CrossRef](#)]
27. Golubkov, A.W.; Scheikl, S.; Planteu, R.; Voitic, G.; Wiltische, H.; Stangl, C.; Fauler, G.; Thaler, A.; Hacker, V. Thermal runaway of commercial 18650 Li-ion batteries with LFP and NCA cathodes—Impact of state of charge and overcharge. *RSC Adv.* **2015**, *5*, 57171–57186. [[CrossRef](#)]
28. Hewson, J.C. Understanding the Limits of the Thermal Runaway in Lithium-Ion-Batteries. Sandia National Laboratories. 2016. Available online: <https://www.osti.gov/servlets/purl/1420927> (accessed on 19 December 2020)
29. Diaz, F.; Wang, Y.; Weyhe, R.; Friedrich, B. Gas-generation measurement and evaluation during mechanical processing and thermal treatment of spent Li-ion batteries. *Waste Manag.* **2019**, *84*, 102–111. [[CrossRef](#)]
30. Essl, C.; Golubkov, A.W.; Fuchs, A. Comparing Different Thermal Runaway Triggers for Two Automotive Lithium-Ion Battery Cell Types. *J. Electrochem. Soc.* **2020**, *167*, 130542. [[CrossRef](#)]
31. Schmidt, J.P.; Arnold, S.; Loges, A.; Werner, D.; Wetzl, T.; Ivers-Tiffée, E. Measurement of the internal cell temperature via impedance: Evaluation and application of a new method. *J. Power Sources* **2013**, *243*, 110–117. [[CrossRef](#)]
32. Zhao, R.; Liu, J.; Gu, J. A comprehensive study on Li-ion battery nail penetrations and the possible solutions. *Energy* **2017**, *123*, 392–401. [[CrossRef](#)]
33. Feng, X.; Sun, J.; Ouyang, M.; He, X.; Lu, L.; Han, X.; Fang, M.; Peng, H. Characterization of large format lithium ion battery exposed to extremely high temperature. *J. Power Sources* **2014**, *272*, 457–467. [[CrossRef](#)]
34. Stephens, D.; Shawcross, P.; Stout, G.; Sullivan, E.; Saunders, J.; Risser, S. *Assessment of Potential Lithium-Ion Battery Safety Issues for Electric and Plug-in Hybrid Vehicles: Report No. DOT HS 812 418*; National Highway Traffic Safety Administration: Washington, DC, USA, 2017.
35. Sidhu, A.; Izadian, A.; Anwar, S. Adaptive Nonlinear Model-Based Fault Diagnosis of Li-Ion Batteries. *IEEE Trans. Ind. Electron.* **2015**, *62*, 1002–1011. [[CrossRef](#)]
36. Srinivasan, R.; Demirev, P.A.; Carkhuff, B.G. Rapid monitoring of impedance phase shifts in lithium-ion batteries for hazard prevention. *J. Power Sources* **2018**, *405*, 30–36. [[CrossRef](#)]
37. Käbitz, S. Untersuchung der Alterung von Lithium-Ionen-Batterien Mittels Elektroanalytik und Elektrochemischer Impedanzspektroskopie. Ph.D. Thesis, RWTH Aachen, Aachen, Germany, 2016.

38. Feng, X.; Zheng, S.; He, X.; Wang, L.; Wang, Y.; Ren, D.; Ouyang, M. Time Sequence Map for Interpreting the Thermal Runaway Mechanism of Lithium-Ion Batteries With $\text{LiNi}_x\text{Co}_y\text{Mn}_z\text{O}_2$ Cathode. *Front. Energy Res.* **2018**, *6*, 264. [[CrossRef](#)]
39. Cai, T.; Stefanopoulou, A.G.; Siegel, J.B. Modeling Li-Ion Battery Temperature and Expansion Force during the Early Stages of Thermal Runaway Triggered by Internal Shorts. *J. Electrochem. Soc.* **2019**, *166*, A2431–A2443. [[CrossRef](#)]
40. Wang, Q.; Mao, B.; Stolarov, S.I.; Sun, J. A review of lithium ion battery failure mechanisms and fire prevention strategies. *Prog. Energy Combust. Sci.* **2019**, *73*, 95–131. [[CrossRef](#)]
41. Spotnitz, R.; Franklin, J. Abuse behavior of high-power, lithium-ion cells. *J. Power Sources* **2003**, *113*, 81–100. [[CrossRef](#)]
42. Zhang, Y.; Wang, H.; Wang, Y.; Li, C.; Liu, Y.; Ouyang, M. Thermal abusive experimental research on the large-format lithium-ion battery using a buried dual-sensor. *J. Energy Storage* **2021**, *33*, 102156. [[CrossRef](#)]
43. Mier, F.A. *Measurement of 18650 Format Lithium Ion Battery Vent Mechanism Flow Parameters*; Masterarbeit; New Mexico Institute of Mining and Technology: Socorro, NM, USA, 2018.
44. Nascimento, M.; Novais, S.; Ding, M.S.; Ferreira, M.S.; Koch, S.; Passerini, S.; Pinto, J.L. Internal strain and temperature discrimination with optical fiber hybrid sensors in Li-ion batteries. *J. Power Sources* **2019**, *410–411*, 1–9. [[CrossRef](#)]
45. Lei, B.; Zhao, W.; Ziebert, C.; Uhlmann, N.; Rohde, M.; Seifert, H. Experimental Analysis of Thermal Runaway in 18650 Cylindrical Li-Ion Cells Using an Accelerating Rate Calorimeter. *Batteries* **2017**, *3*, 14. [[CrossRef](#)]
46. Chen, M.; Liu, J.; He, Y.; Yuen, R.; Wang, J. Study of the fire hazards of lithium-ion batteries at different pressures. *Appl. Therm. Eng.* **2017**, *125*, 1061–1074. [[CrossRef](#)]
47. Feng, X.; Ren, D.; He, X.; Ouyang, M. Mitigating Thermal Runaway of Lithium-Ion Batteries. *Joule* **2020**, *4*, 743–770. [[CrossRef](#)]
48. Bandhauer, T.M.; Garimella, S.; Fuller, T.F. A Critical Review of Thermal Issues in Lithium-Ion Batteries. *J. Electrochem. Soc.* **2011**, *158*, R1. [[CrossRef](#)]
49. Rao, Z.; Wang, S. A review of power battery thermal energy management. *Renew. Sustain. Energy Rev.* **2011**, *15*, 4554–4571. [[CrossRef](#)]
50. Thakur, A.K.; Prabakaran, R.; Elkadeem, M.R.; Sharshir, S.W.; Arıcı, M.; Wang, C.; Zhao, W.; Hwang, J.Y.; Saidur, R. A state of art review and future viewpoint on advance cooling techniques for Lithium-ion battery system of electric vehicles. *J. Energy Storage* **2020**, *32*, 101771. [[CrossRef](#)]
51. Madani, S.; Schaltz, E.; Knudsen Kær, S. An Electrical Equivalent Circuit Model of a Lithium Titanate Oxide Battery. *Batteries* **2019**, *5*, 31. [[CrossRef](#)]
52. Zhang, S.S. A review on the separators of liquid electrolyte Li-ion batteries. *J. Power Sources* **2007**, *164*, 351–364. [[CrossRef](#)]
53. Hu, X.; Zhang, K.; Liu, K.; Lin, X.; Dey, S.; Onori, S. Advanced Fault Diagnosis for Lithium-Ion Battery Systems: A Review of Fault Mechanisms, Fault Features, and Diagnosis Procedures. *IEEE Ind. Electron. Mag.* **2020**, *14*, 65–91. [[CrossRef](#)]
54. Chen, Z.; Xu, K.; Wei, J.; Dong, G. Voltage fault detection for lithium-ion battery pack using local outlier factor. *Measurement* **2019**, *146*, 544–556. [[CrossRef](#)]
55. Yao, L.; Xiao, Y.; Gong, X.; Hou, J.; Chen, X. A novel intelligent method for fault diagnosis of electric vehicle battery system based on wavelet neural network. *J. Power Sources* **2020**, *453*, 227870. [[CrossRef](#)]
56. Chen, Z.; Xiong, R.; Tian, J.; Shang, X.; Lu, J. Model-based fault diagnosis approach on external short circuit of lithium-ion battery used in electric vehicles. *Appl. Energy* **2016**, *184*, 365–374. [[CrossRef](#)]
57. Zhu, S.; Han, J.; An, H.Y.; Pan, T.S.; Wei, Y.M.; Song, W.L.; Chen, H.S.; Fang, D. A novel embedded method for in situ measuring internal multi-point temperatures of lithium ion batteries. *J. Power Sources* **2020**, *456*, 227981. [[CrossRef](#)]
58. Wang, Z.R.; Yang, Y.; Tong, X. Lithium-Ion Battery Pack Thermal Runaway Automatic Alarming Apparatus Based on Gas Monitoring and Monitoring Method. Chinese Patent 108008083A, 8 May 2018.
59. Finegan, D.P.; Darcy, E.; Keyser, M.; Tjaden, B.; Heenan, T.M.M.; Jarvis, R.; Bailey, J.J.; Malik, R.; Vo, N.T.; Magdysyuk, O.V.; et al. Characterising thermal runaway within lithium-ion cells by inducing and monitoring internal short circuits. *Energy Environ. Sci.* **2017**, *10*, 1377–1388. [[CrossRef](#)]
60. Finegan, D.P.; Darst, J.; Walker, W.; Li, Q.; Yang, C.; Jarvis, R.; Heenan, T.M.; Hack, J.; Thomas, J.C.; Rack, A.; et al. Modelling and experiments to identify high-risk failure scenarios for testing the safety of lithium-ion cells. *J. Power Sources* **2019**, *417*, 29–41. [[CrossRef](#)]
61. Dey, S.; Perez, H.E.; Moura, S.J. Thermal fault diagnostics in Lithium-ion batteries based on a distributed parameter thermal model. In Proceedings of the 2017 American Control Conference (ACC), Seattle, WA, USA, 24–26 May 2017; pp. 68–73.
62. Hong, J.; Wang, Z.; Liu, P. Big-Data-Based Thermal Runaway Prognosis of Battery Systems for Electric Vehicles. *Energies* **2017**, *10*, 919. [[CrossRef](#)]
63. Jiang, L.; Deng, Z.; Tang, X.; Hu, L.; Lin, X.; Hu, X. Data-driven fault diagnosis and thermal runaway warning for battery packs using real-world vehicle data. *Energy* **2021**, *234*, 1–11. [[CrossRef](#)]
64. Wang, Z.; Hong, J.; Liu, P.; Zhang, L. Voltage fault diagnosis and prognosis of battery systems based on entropy and Z-score for electric vehicles. *Appl. Energy* **2017**, *196*, 289–302. [[CrossRef](#)]
65. Li, X.; Dai, K.; Wang, Z.; Han, W. Lithium-ion batteries fault diagnostic for electric vehicles using sample entropy analysis method. *J. Energy Storage* **2020**, *27*, 1–11. [[CrossRef](#)]
66. Liu, P.; Sun, Z.; Wang, Z.; Zhang, J. Entropy-Based Voltage Fault Diagnosis of Battery Systems for Electric Vehicles. *Energies* **2018**, *11*, 136. [[CrossRef](#)]

67. Koch, S.; Birke, K.; Kuhn, R. Fast Thermal Runaway Detection for Lithium-Ion Cells in Large Scale Traction Batteries. *Batteries* **2018**, *4*, 16. [CrossRef]
68. Klink, J.; Grabow, J.; Orazov, N.; Bengler, R.; Börger, A.; Ahlberg Tidblad, A.; Wenzl, H.; Beck, H.P. Thermal fault detection by changes in electrical behaviour in lithium-ion cells. *J. Power Sources* **2021**, *490*, 229572. [CrossRef]
69. German Institute for Standardization. *Electrically Propelled Road Vehicles—Battery Systems—Design Specifications for Lithium-Ion Battery Cells*; German Institute for Standardization: Berlin, Germany, 2016.
70. Kohlberg, M. Safety Element for Battery Cell. US Patent US 10.026.948 B2, 10 March 2014.
71. Spies, P. Flexible Battery Management System with Active Cell Balancing (FlexBMS): Preliminary, 2015. Available online: https://www.mikroelektronik.fraunhofer.de/content/dam/mikroelektronik/Datenbltter/IIS_Batteriemangement_DB.pdf (accessed on 17 January 2022).
72. UN Global Technical Regulation. Proposal for Amendment 4 to UN GTR No. 4 (WHDC), Genf, CH, 2021. Available online: https://unece.org/sites/default/files/2021-06/ECE_TRANS_WP.29_2021_79E.pdf (accessed on 8 February 2022).
73. Ruiz, V.; Pfrang, A.; Kriston, A.; Omar, N.; van den Bossche, P.; Boon-Brett, L. A review of international abuse testing standards and regulations for lithium ion batteries in electric and hybrid electric vehicles. *Renew. Sustain. Energy Rev.* **2018**, *81*, 1427–1452. [CrossRef]
74. Melcher, A.; Ziebert, C.; Rohde, M.; Seifert, H. Modeling and Simulation of the Thermal Runaway Behavior of Cylindrical Li-Ion Cells—Computing of Critical Parameters. *Energies* **2016**, *9*, 292. [CrossRef]
75. MathWorks. Matlab/Simulink, MathWorks Inc., 2019. Available online: https://de.mathworks.com/products/new_products/release2019a.html (accessed on 8 February 2022).
76. Zhang, H.; Chow, M.Y. Comprehensive dynamic battery modeling for PHEV applications. In Proceedings of the IEEE PES General Meeting, Minneapolis, MN, USA, 25–29 July 2010; pp. 1–6. [CrossRef]
77. Roscher, M.A.; Sauer, D.U. Dynamic electric behavior and open-circuit-voltage modeling of LiFePO₄-based lithium ion secondary batteries. *J. Power Sources* **2011**, *196*, 331–336. [CrossRef]
78. Qin, P.; Sun, J.; Wang, Q. A new method to explore thermal and venting behavior of lithium-ion battery thermal runaway. *J. Power Sources* **2021**, *486*, 229357. [CrossRef]
79. Dey, S.; Perez, H.E.; Moura, S.J. Model-Based Battery Thermal Fault Diagnostics: Algorithms, Analysis, and Experiments. *IEEE Trans. Control. Syst. Technol.* **2019**, *27*, 576–587. [CrossRef]
80. Tran, M.K.; Fowler, M. A Review of Lithium-Ion Battery Fault Diagnostic Algorithms: Current Progress and Future Challenges. *Algorithms* **2020**, *13*, 62. [CrossRef]
81. Challa, V. How to Prevent Li-Ion Battery Failures, Beltsville, MD, 2018. Available online: https://www.dfrsolutions.com/hubfs/2018%20DFR%20Conference%20Presentations/Tutorial%204_How%20to%20Qualify%20Your%20Batteries%20to%20Prevent%20Failures%20and%20Thermal%20Events.pdf (accessed on 4 January 2020).
82. Chen, Y.; Kang, Y.; Zhao, Y.; Wang, L.; Liu, J.; Li, Y.; Liang, Z.; He, X.; Li, X.; Tavajohi, N.; et al. A review of lithium-ion battery safety concerns: The issues, strategies, and testing standards. *J. Energy Chem.* **2021**, *59*, 83–99. [CrossRef]
83. Feng, X.; Ouyang, M.; Liu, X.; Lu, L.; Xia, Y.; He, X. Thermal runaway mechanism of lithium ion battery for electric vehicles: A review. *Energy Storage Mater.* **2018**, *10*, 246–267. [CrossRef]
84. Zhang, M.; Liu, L.; Stefanopoulou, A.G.; Siegel, J.; Lu, L.; He, X.; Ouyang, M. Fusing Phenomenon of Lithium-Ion Battery Internal Short Circuit. *J. Electrochem. Soc.* **2017**, *164*, A2738–A2745. [CrossRef]
85. Liu, B.; Jia, Y.; Yuan, C.; Wang, L.; Gao, X.; Yin, S.; Xu, J. Safety issues and mechanisms of lithium-ion battery cell upon mechanical abusive loading: A review. *Energy Storage Mater.* **2020**, *24*, 85–112. [CrossRef]
86. Liu, L.; Feng, X.; Zhang, M.; Lu, L.; Han, X.; He, X.; Ouyang, M. Comparative study on substitute triggering approaches for internal short circuit in lithium-ion batteries. *Appl. Energy* **2020**, *259*. [CrossRef]
87. Essl, C.; Seifert, L.; Rabe, M.; Fuchs, A. Early Detection of Failing Automotive Batteries Using Gas Sensors. *Batteries* **2021**, *7*, 25. [CrossRef]
88. Liao, Z.; Zhang, S.; Li, K.; Zhang, G.; Habetler, T.G. A survey of methods for monitoring and detecting thermal runaway of lithium-ion batteries. *J. Power Sources* **2019**, *436*, 226879. [CrossRef]
89. Popp, H.; Koller, M.; Jahn, M.; Bergmann, A. Mechanical methods for state determination of Lithium-Ion secondary batteries: A review. *J. Energy Storage* **2020**, *32*, 101859. [CrossRef]
90. Alavi, S.M.M.; Fekriasl, S.; Niyakan, S.N.; Saif, M. Fault detection and isolation in batteries power electronics and chargers. *J. Energy Storage* **2019**, *25*, 100807. [CrossRef]
91. Feng, X.; Weng, C.; Ouyang, M.; Sun, J. Online internal short circuit detection for a large format lithium ion battery. *Appl. Energy* **2016**, *161*, 168–180. [CrossRef]
92. Kang, Y.; Duan, B.; Zhou, Z.; Shang, Y.; Zhang, C. A multi-fault diagnostic method based on an interleaved voltage measurement topology for series connected battery packs. *J. Power Sources* **2019**, *417*, 132–144. [CrossRef]
93. Cheng, Z.; Walid, A.; Quang, D.; Pedro, A.; James, M. Online estimation of battery equivalent circuit model parameters and state of charge using decoupled least squares technique. *Energy* **2018**, *142*, 678–688. [CrossRef]